CrossMark

On the Magnetic Nature of an Exploding Granule as Revealed by Sunrise/IMaX

Salvo L. Guglielmino[1] , Valentín Martínez Pillet[2] , Basilio Ruiz Cobo[3,4] , Luis R. Bellot Rubio[5] ,
José Carlos del Toro Iniesta[5] , Sami K. Solanki[6,7], Tino L. Riethmüller[6] , and Francesca Zuccarello[1]
[1] Dipartimento di Fisica e Astronomia "Ettore Majorana"—Sezione Astrofisica, Università degli Studi di Catania, Via S. Sofia 78, I-95123 Catania, Italy
salvatore.guglielmino@inaf.it
[2] NSO—National Solar Observatory 3665 Discovery Drive, Boulder, CO 80303, USA
[3] IAC—Instituto de Astrofísica de Canarias, C/Vía Láctea s/n, E-38200, La Laguna, Tenerife, Spain
[4] ULL—Departamento de Astrofísica, Univ. de La Laguna, E-38205, La Laguna, Tenerife, Spain
[5] IAA—Instituto de Astrofísica de Andalucía (CSIC), Apdo. de Correos 3004, E-18080 Granada, Spain
[6] Max-Planck-Institut für Sonnensystemforschung, Justus-von-Liebig-Weg 3, D-37077 Göttingen, Germany
[7] School of Space Research, Kyung Hee University, Yongin, Gyeonggi-Do, 446-701, Republic of Korea

Abstract

We study the photospheric evolution of an exploding granule observed in the quiet Sun at high spatial ($\sim$0″3) and temporal (31.5 s) resolution by the imaging magnetograph SUNRISE/IMaX in 2009 June. These observations show that the exploding granule is cospatial to a magnetic flux emergence event occurring at mesogranular scale (up to $\sim$12 Mm^2 area). Using a modified version of the SIR code for inverting the IMaX spectropolarimetric measurements, we obtain information about the magnetic configuration of this photospheric feature. In particular, we find evidence of highly inclined emerging fields in the structure, carrying a magnetic flux content up to $\sim$4 $\times$ 10^{18} Mx. The balance between gas and magnetic pressure in the region of flux emergence, compared with a very quiet region of the Sun, indicates that the additional pressure carried by the emerging flux increases the total pressure by about 5% and appears to allow the granulation to be modified, as predicted by numerical simulations. The overall characteristics suggest that a multipolar structure emerges into the photosphere, resembling an almost horizontal flux sheet. This seems to be associated with exploding granules. Finally, we discuss the origin of such flux emergence events.

1. Introduction

A typical phenomenon observed in the quiet-Sun granulation pattern is the appearance of exploding granules (EGs). These are individual bright granules that expand more than normal granular cells, and ultimately fragment into several smaller granules. They have a rather long lifetime, with an average value of $\approx$9 minutes, and reach a maximum diameter of about 4″–5″ (Mehltretter 1978; Title et al. 1989; Rast 1995).

Since the first detection of EGs (Rösch 1960), a number of studies analyzed their dynamics and physical properties from both the observational point of view (Carlier et al. 1968; Namba & Diemel 1969; Allen & Musman 1973; Namba & van Rijsbergen 1977; Mehltretter 1978; Kitai & Kawaguchi 1979; Namba 1986; Title et al. 1989; Hirzberger et al. 1997, 1999a, 1999b, 2001; Roudier et al. 2001; Berrilli et al. 2002; Vargas Domínguez et al. 2010; Palacios et al. 2012; Sobotka et al. 2012; Fischer et al. 2017) and numerical modeling (e.g., Musman 1972; Nelson & Musman 1978; Nordlund 1985; Simon & Weiss 1991; Rast 1995; Stein & Nordlund 1998; see also the review of Nordlund et al. 2009 and the recent simulations by Moreno-Insertis et al. 2018; Rempel 2018).

Regular granules can be divided into two populations, with diameters smaller than and larger than 1″4, respectively (e.g., Hirzberger et al. 1997; Gadun et al. 2000; Berrilli et al. 2002; Yu et al. 2011). Small and large granules exhibit differences in the geometrical and brightness structure and in the temporal evolution (Hirzberger et al. 1997, 1999a). EGs belong to the family of large granules because they die by fragmentation and have the longest mean lifetime. Like in large granules, in EGs the brightest parts and maximum upward velocity are also shifted toward the granular boundaries (Hirzberger 2002). Temporal sequences of white-light high-resolution observations showed that EGs are not rare: their number density is about 4% of the observed area of the photosphere (Mehltretter 1978). Later works found slightly lower values: EGs covered about 2.5% of the photosphere (Namba 1986; Title et al. 1989).

Exploding granules often exhibit a central dark spot, as first described by Kitai & Kawaguchi (1979). The possible connection of this dark hub with downflows of cool gas within the granules was suggested by Hirzberger et al. (1999b). Two-dimensional spectroscopic measurements confirmed the existence of such downflows in the central area (Hirzberger et al. 2001; Roudier et al. 2001; Berrilli et al. 2002). The dark center of EGs is interpreted to be a result of buoyancy braking (Massaguer & Zahn 1980). The pressure near the center of granules increases while sustaining their horizontal radial flows to conserve mass. The enhanced pressure reduces the upflow and heat transport to the surface. This process produces a stagnation point, which rapidly cools down and eventually

reverses the flow, leading to the formation of the observed dark central feature, which is characterized by downward velocity while the EG starts splitting (Nelson & Musman 1978).

The explosion of an EG can occur in a recurrent way, with some fragments that explode again (Oda 1984; Namba 1986). For this reason, EGs represent the most vigorous manifestation of fragmenting granules (Roudier et al. 2003). This behavior was already noticed by Kawaguchi (1980) for granules with diameters greater than 2″, but for EGs, it was further related to mesogranulation in observations (e.g., Rieutord et al. 2000; Berrilli et al. 2005) and numerical models (November et al. 1981; Oda 1984; Simon et al. 1991; Ploner et al. 2000). In particular, it was observed that small convective elements (granules) superimposed on larger cells (mesogranules), randomly distributed, may give rise to the formation of EGs (Simon & Weiss 1991). In this context, areas of positive divergence of the horizontal velocity, which form the mesogranular pattern found in hydrodynamical simulations (Rast 2003; Matloch et al. 2009, 2010), are identified with EGs in observations (e.g., Domínguez Cerdeña 2003; Roudier et al. 2003; Roudier & Muller 2004).

In spite of the detailed knowledge of the morphological evolution of EGs, their correlation with magnetic flux emergence episodes is not well settled. De Pontieu (2002) found the presence of emerging flux in certain EGs, suggesting the presence of mostly horizontal magnetic fields. He related these flux emergence events with the so-called horizontal internetwork fields (HIFs) that were discovered by Lites et al. (1996). Moreover, Socas-Navarro et al. (2004), analyzing low-flux signals in internetwork regions, pointed out a scenario compatible with emergence of flux at granular scale. More recently, Orozco Suárez et al. (2008) showed individual cases of magnetic flux emergence in granules with full Stokes polarimetry at high spatial and temporal resolution. Zhang et al. (2009) observed flux emergence as a cluster of mixed polarities following the splitting of a large granule. Palacios et al. (2012) investigated the evolution of two mesogranular-scale EGs, finding that weak unipolar longitudinal fields appear first. These magnetic flux concentrations were followed by the appearance of the opposite polarity and developed into intergranular lanes, while the transverse field remained almost negligible in the flux concentration where it could be measured.

In this paper, we benefit from observations of the solar photosphere taken by the Imaging Magnetograph eXperiment (IMaX; Martínez Pillet et al. 2011) on board the SUNRISE balloon-borne solar observatory (Solanki et al. 2010, 2017; Barthol et al. 2011; Berkefeld et al. 2011; Gandorfer et al. 2011). The high spatial resolution and polarimetric sensitivity of the magnetograms acquired by IMaX shed light on the evolution of several types of small-scale magnetic features in the quiet Sun. Indeed, it provided a rich picture of the dynamic processes that involve individual magnetic elements in the photosphere (e.g., emergence of small loops, Danilovic et al. 2010; Guglielmino et al. 2012; convective collapse, Requerey et al. 2014, 2015; dynamics of magnetic bright points, Jafarzadeh et al. 2013, 2014; Utz et al. 2014; for a statistical analysis, see Anusha et al. 2017). Furthermore, IMaX measurements allowed magnetic flux tubes to be spatially resolved in the internetwork (Lagg et al. 2010) and network (Martínez González et al. 2012a).

In the present work, we analyze at high spatial and temporal resolution the evolution of an EG that is cospatial to a flux emergence event occurring at mesogranular scale. We study this emerging flux region, which has been described by Palacios et al. (2012), complementing the analysis with new information concerning the characterization and distribution of the polarization signals across the feature and its thermo-dynamical properties. Section 2 describes the observations and the methods that we used for the data analysis. In Section 3 we report our results, discussing them in comparison with magnetohydrodynamical (MHD) simulations in Section 4. Finally, Section 5 summarizes our results and places them in a more general context.
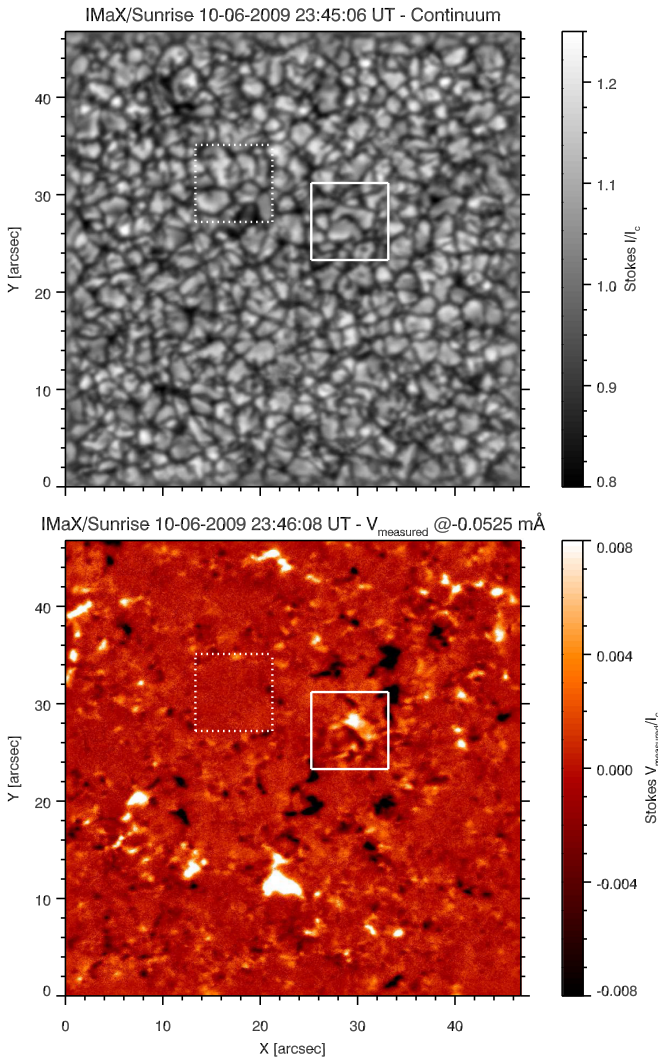
2. Observations, Methods, and Data Analysis

We have analyzed a spectropolarimetric IMaX data set obtained on 2009 June 10, 22:55:41–23:54:30 UT, during the first science flight of the SUNRISE observatory. During that time, IMaX took polarization maps at twelve wavelength positions over the Fe I 525.02 nm line (Landé factor $g = 3$) every 3.5 pm from $\lambda = -19.25$ pm to $\lambda = +19.25$ pm with respect to the line center, with a spectral resolution of 8.5 pm. Two images were accumulated per wavelength point by performing measurements of the Stokes parameters I and V only (longitudinal L12-2 observing mode). The pixel size of the maps is 0.″055. The field of view (FoV) covered by these observations is about $46″ \times 46″$ over a quiet-Sun region at the disk center, as shown in Figure 1. The temporal cadence of the acquisition was 31.5 s.

Data have been processed for dark-current subtraction and flat-field correction. Two different types of data have been produced: non-reconstructed (level 1) and reconstructed (level 2), the latter being obtained by using phase-diversity information and taking into account the wavefront correction (Berkefeld et al. 2011). The spatial resolution is 0.″3 (level 1) and 0.″23 (level 2), respectively. The same data set was analyzed by Riethmüller et al. (2014) to study bright points. We refer to that paper for information on the data and the observed region. Further details about data reduction are provided by Martínez Pillet et al. (2011). In the following, we use the level 1 data, which ensures a signal-to-noise ratio of about 1.2×10^{-3} in units of the continuum intensity I_c per wavelength point in Stokes V. The rms contrast of the granulation in the continuum is 7% for these level 1 data.

I_c has been computed by averaging the Stokes I intensities at $\lambda = \pm 19.25$ pm from the line center. The resulting I_c maps have been used to align the observational sequence referring to the flux emergence event. Some slight displacements of the FoV occurred during the observing interval because of short glitches of the image stabilization system. Therefore we have used a cross-correlation algorithm to track the EG between the observational gaps. The total length of the analyzed time series is about 17.5 minutes.

2.1. Polarization Cross-talk

While using longitudinal IMaX observing modes, such as the L12-2 mode, it is not possible to correct for instrumental cross-talk by applying the demodulation matrix described by Martínez Pillet et al. (2011), which takes into account the polarization effect induced by the telescope and by the image stabilization and light distribution system (ISLiD; Gandorfer et al. 2011). This implies that a conspicuous cross-talk between the Stokes parameters still remains in the reduced data.

IMaX/Sunrise 10-06-2009 23:45:06 UT - Continuum

IMaX/Sunrise 10-06-2009 23:46:08 UT - V_{measured} @-0.0525 mÅ

Figure 1. Top panel: continuum intensity map. Bottom panel: V_{measured} signal map in the blue lobe of the observed Stokes V. They cover the FoV of IMaX of about $46'' \times 46''$. The solid square, with a subFoV of $\sim 8'' \times 8''$, indicates the location of the emerging flux region. The dashed square, with the same subFoV, indicates a region of very quiet Sun that we used as a control box for comparison.

An estimate of the cross-talk for Stokes V, obtained from a measurement performed just before the flight of the SUNRISE balloon, is given by

$$V_{\mathrm{measured}} = -0.88\, U_{\mathrm{source}} + 0.55\, V_{\mathrm{source}}, \qquad (1)$$

where U_{source} and V_{source} refer to the calibration source. The cross-talk originates mostly from the two folding mirrors behind the primary mirror, M3 and M4, and the ISLiD. Hence, the observed Stokes V signal does not represent the real circular polarization signal.

An additional problem is that we lack pointing information for these IMaX observations, so we cannot set a reference frame for the Stokes vector in which Stokes $Q_{\odot} = 0$, e.g., at solar west, indicating with subscript $\odot$ the original solar signals in such a reference frame. That is, in general, we should represent the emerging observed Stokes Q and U parameters as a linear combination of Stokes $Q_{\odot}$ and $U_{\odot}$, respectively.

In general, there is a rotation between Q_{source} and U_{source} to $Q_{\odot}$ and $U_{\odot}$ that one needs to know carefully to provide

magnetic field directions on the plane of the sky. However, as shown in Section 2.2 and in the Appendix, the inversion procedure we use does not determine the azimuth (or B_{tran}) in any reliable way. Thus, the additional rotation to provide orientations in the plane of the sky is not used in this paper, and without losing generality, we can therefore write Equation (1) as

$$V_{\mathrm{measured}} = -0.88\, U_{\odot} + 0.55\, V_{\odot}. \qquad (2)$$

Equation (2) describes the observed Stokes V signal as a linear combination of Stokes $U_{\odot}$ and $V_{\odot}$ that is suitable for investigating linear and longitudinal polarization signals in the EG.

Typically, the Zeeman effect produces only weak linear polarization signals in the quiet Sun. As a consequence, to zeroth order, the contribution of Stokes $U_{\odot}$ can be neglected and V_{measured} can be considered as a measure of the original Stokes $V_{\odot}$, with a reduced amplitude by a factor of about 1.8. This assumption is a reasonable guess, for instance, in network elements where vertical fields are expected, as illustrated by Martínez González et al. (2012a). A clear relationship between inclination and field strength is shown by Riethmüller & Solanki (2017): only weak fields are horizontal, and their Stokes Q and U signals are really small (see also Danilovic et al. 2010 for the typical strength of Stokes Q and U signals). Conversely, this assumption is broken in regions close to neutral lines, where Stokes $U_{\odot}$ becomes stronger than Stokes $V_{\odot}$.

Let us now consider the integrated signal of V_{measured} averaged over the line, given by

$$V_{\mathrm{integrated}} = \frac{1}{8\langle I_c \rangle} \sum_{i=1}^{8} \epsilon_i V_{\mathrm{measured}}|_i, \qquad (3)$$

where $\langle I_c \rangle$ is the continuum intensity averaged over the IMaX FoV, i runs over the central eight wavelength positions, from $\lambda = -12.25$ pm to $\lambda = +12.25$ pm with respect to the line center, with $\epsilon = 1$ for the first four positions and $\epsilon = -1$ for the other four positions. As a first approximation, this quantity is null only in the regions where the magnetic field is zero or is horizontal (changing sign), i.e., where the integrated Stokes $V_{\odot}$ signal is zero, as long as Stokes $U_{\odot}$ is symmetric in wavelength while Stokes $V_{\odot}$ antisymmetric (Landi Degl'Innocenti 1992). In this respect, $V_{\mathrm{integrated}}$ represents the distribution of the magnetic areas fairly well. Neutral lines derived with this method, although they are regions that are more affected by the cross-talk, are a good proxy for the real neutral lines. However, we cannot have any knowledge of the magnetic flux from Equation (3).

2.2. SirUV Code

The presence of a residual cross-talk for Stokes V prevents us from using the standard procedures of data analysis. In fact, the inversion of the spectra as they are measured would fail to retrieve the correct values of various physical parameters (i.e., magnetic flux, magnetic field strength B, and inclination γ[8]).

---

[8] The inclination is measured relative to the line of sight, so that 0° indicates a magnetic field vector pointing to the observer, i.e., directed outward from the solar surface at the disk center.

In order to extract more information from the IMaX spectropolarimetric measurements, we have carried out a nonstandard inversion of the observed level 1 spectra by using a modified version of the SIR code (Ruiz Cobo & del Toro Iniesta 1992). This code provides a numerical solution to the radiative transfer equation along the line of sight (LOS) for Zeeman-polarized radiation under the assumption of local thermodynamic equilibrium, minimizing the differences between the observed and the computed synthetic Stokes profiles using response functions. The present version, hereafter SirUV, allows the user to invert any linear combination of the four Stokes parameters.

In the Appendix, we have assessed the capabilities of this SirUV code using IMaX V5–6 (full vector) observations. In summary, this analysis shows that the code retrieves reliable values for the thermodynamical parameters, such as the temperature T and the gas pressure P_{gas}. In addition, the longitudinal component of the magnetic field B_{long} is reasonably well determined. Conversely, the transverse component of the magnetic field B_{tran} remains completely undetermined, and B is not determined to any useful level, with a tendency for it to be overestimated, likely because of the noise (Borrero & Kobel 2011, 2012).

2.3. Data Analysis

After verifying the capabilities of the SirUV code and the reliability of the results that are inferred, as explained in the Appendix, we have carried out the inversion of two subFoVs of 144×144 pixels. The first (FoV$_{\mathrm{EG}}$) covers the EG, the second (FoV$_{\mathrm{QS}}$) is occupied by a region of very quiet Sun, which can be termed a dead-calm region (Martínez González et al. 2012b), as indicated in Figure 1 with solid and dashed boxes, respectively. All the frames relevant to FoV$_{\mathrm{EG}}$ have been inverted, using the maximum cadence of 31.5 s, while only every fifth frame relevant to FoV$_{\mathrm{QS}}$ has been inverted, with a cadence of $\sim$2.5 minutes, during the observing period when it was included in the full IMaX FoV.

As regards the stratification and the number of nodes used for the inversion, we have taken the same parameters used in the preliminary test. That is, we have used three iteration cycles, with up to four nodes for the temperature T, two nodes for the LOS velocity v_{LOS} and B, and one node for the other parameters. Under the assumption of unity for the magnetic filling factor, in the following, we consider the values of B_{long} in terms of magnetic flux density.

Given the large uncertainty of the v_{LOS} values retrieved by the SirUV inversion, the LOS velocity has been derived from a Gaussian fit to the 12 points along the observed Stokes I profile, considering the Doppler shift with respect to the line center. The blueshift over the FoV due to the collimated setup of the Fabry-Pérot etalon of the magnetograph has also been removed in the inferred velocity values. Taking into account that the random superposition of solar acoustic oscillation coherence patches and underlying convective flows may introduce a bias in the interpretation of the Doppler velocities in IMaX data (see McClure et al. 2019), we have applied a p-mode filtering. Finally, we have calibrated the velocity scale over the entire FoV by using a convective blueshift (Dravins et al. 1981) of $\sim$200 m s^{-1} for the Fe I 525.02 nm line at disk center, as used for other IMaX data sets (see, e.g., Roth et al. 2010). The typical error of this measure is about $\pm$100 m s^{-1}.

We have also studied the behavior of T, P_{gas}, and of the magnetic pressure $P_{\mathrm{mag}} = B^2/2\mu_0$, where μ_0 is the vacuum permeability. To estimate P_{mag}, we have considered that in the emerging flux region it can be assumed that

$$B_{\mathrm{tran}} \simeq B_{\mathrm{long}},$$

thus

$$P_{\mathrm{mag}} = \frac{B^2}{2\mu_0} = \frac{B_{\mathrm{long}}^2 + B_{\mathrm{tran}}^2}{2\mu_0} \simeq \frac{B_{\mathrm{long}}^2}{\mu_0}.$$

Hence, the quantity depends only on B_{long}, which is a well-determined observable from our spectropolarimetric measurements.

The spatial averages of T, P_{gas}, and P_{mag} have been carried out separately for granules and intergranular lanes. For this purpose, we applied a discrimination based on the continuum brightness of these features. Pixels brighter by at least 4% than their surroundings, considering the average value of a 19×19 pixel box surrounding the point under consideration, are taken to be granules. In the same way, the criterion is used to identify intergranular lanes as pixels that are at least 3% darker than their surroundings.

3. Results

A magnetic flux concentration with a complex mixed-polarity pattern is seen to emerge at 23:36:42 UT ($\Delta t = 0$ s). The feature is clearly recognizable in the full FoV of these IMaX L12-2 observations, as shown in Figure 1 about 9 minutes later. This flux emergence episode, described as "emergence event l10" in Palacios et al. (2012), is found to be associated with an EG.

Figure 2, covering the FoV$_{\mathrm{EG}}$, illustrates the evolution of the EG and of the cospatial emerging flux region, with a cadence of about 4 minutes beginning from $\Delta t = 0$ s. The movie available in the online journal clearly displays the intermediate phases during the evolution of the structure, with the highest temporal cadence (31.5 s), except for two observational gaps. The first gap occurred between $\Delta t \approx 120$ s and $\Delta t \approx 240$ s, whereas the second gap, shorter than the former, lies between $\Delta t = 315$ s and $\Delta t = 378$ s.

The first column of Figure 2 presents the evolution of the photospheric continuum I_c. We can observe that this expanding structure begins to form a central dark spot ($\Delta t = 252$ s), which eventually grows in size while the EG splits into two smaller granules ($\Delta t = 504$ s). Then, the southernmost descendant granule located at $[2'', 4''] \times [2'', 4'']$ undergoes the same evolution ($\Delta t = 756$ s), until it splits into four granules ($\Delta t = 1008$ s).

The second column of Figure 2 shows the integrated signal of V_{measured}. The emerging flux region first appears at $\Delta t = 0$ s, being located at $[5'', 4'']$. Magnetic field patches with apparent opposite polarity appear close to each other. These magnetic patches expand and occupy the EG area ($\Delta t = 252$ s), showing a pattern of alternate polarities (salt-and-pepper or sea-serpent configuration). Some of these flux kernels intensify: notably, this occurs in the region where the first dark spot is forming ($\Delta t = 504$ s). Later, this structure becomes an intergranular lane ($\Delta t = 756$ s).

Doppler velocity maps, displayed in Figure 2 (third column), highlight the plasma motions in the region. They indicate that the structure is generally characterized by conspicuous
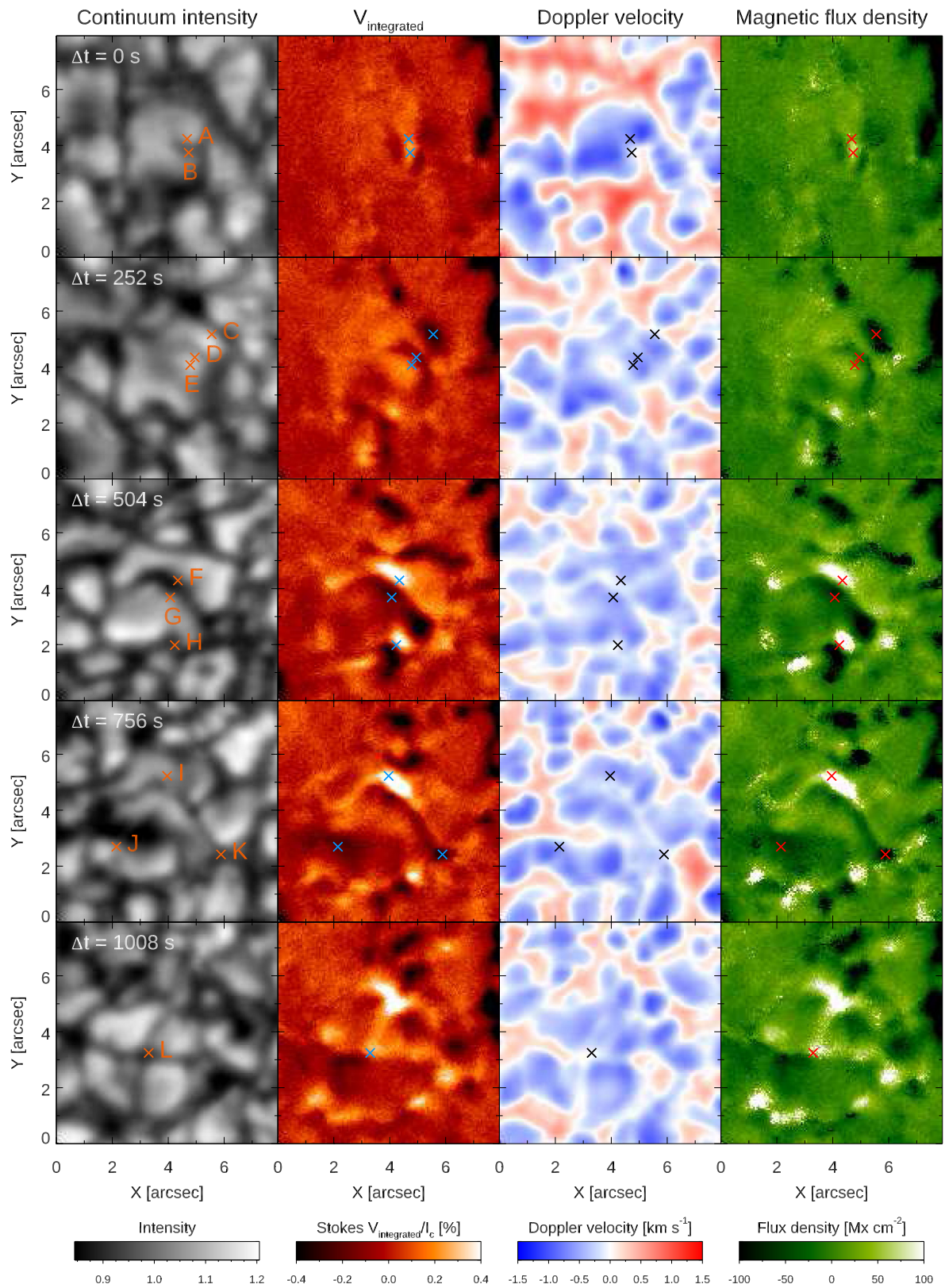
Figure 2. Time sequence of the evolution of the emerging magnetic structure. The FoV is that framed with a solid line box in Figure 1. First column: continuum intensity maps. Second column: observed circular polarization ($V_{observed}$) maps. Third column: Doppler velocity v_{Dopp} maps. Fourth column: magnetic flux density maps. Time runs from top to bottom: the cadence of the sequence is about 4 minutes. Crosses labeled with capital letters indicate pixels whose Stokes profiles are shown in Figure 5. An animation of this figure is available. The video begins at $\Delta t = 0$ s and ends at $\Delta t = 1039.5$ s. The real-time duration of the video is 9 s.

(An animation of this figure is available.)
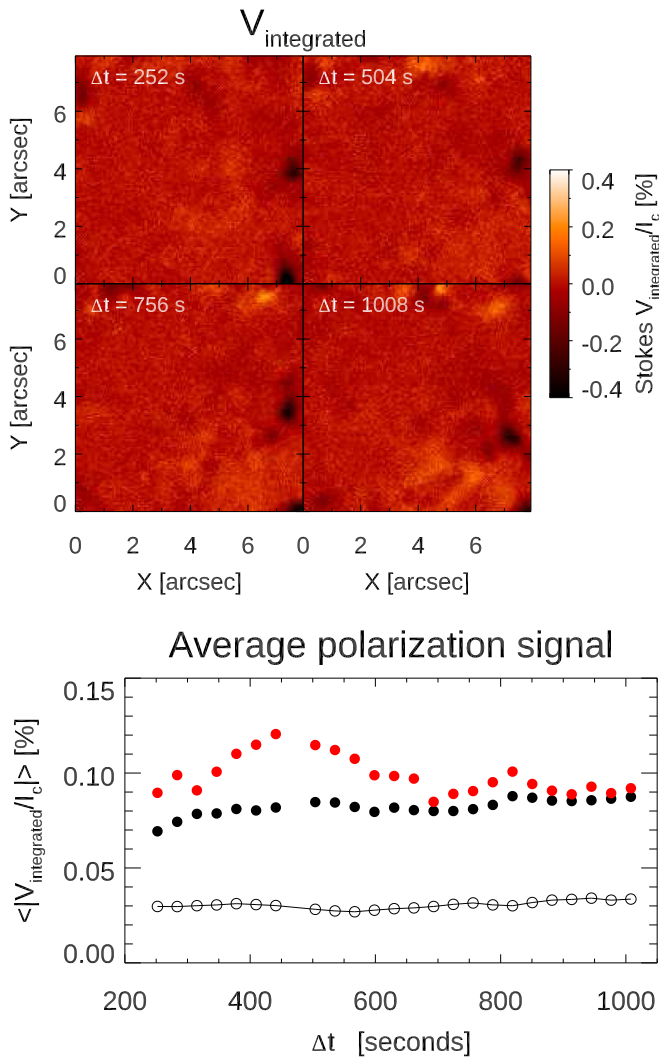
Figure 3. Top panels: observed circular polarization ($V_{observed}$) maps at representative times for FoV_{QS}, which is framed with a dashed line box in Figure 1. Bottom panel: mean value of absolute $V_{integrated}$ over FoV_{EG} (black circles) within the region of interest occupied by the EG inside FoV_{EG} (red circles) and FoV_{QS} (empty circles).

Figure 4. Top panel: plot of the evolution of the total (unsigned) magnetic flux content in the emerging structure cospatial to the EG in the FoV_{EG}. Bottom panel: same for the area covered by magnetic flux emergence.

blueshifts, corresponding to upflows up to 1–1.5 km s^{-1}. In the central dark patch, downflows of $\simeq 0.5$ km s^{-1} are found ($\Delta t = 504$ s and, partly, at $\Delta t = 1008$ s), in agreement with previous observations. The same coherent behavior is also visible in the online movie.

The maps of magnetic flux density (Figure 2, fourth column) reveal that the distribution of the magnetic areas derived from $V_{integrated}$ is representative of the real magnetic flux patches. Indeed, a mixture of polarities is found where $V_{integrated}$ maps show an apparent salt-and-pepper configuration, suggesting once again that the quantity described in Equation (3) is a good qualitative proxy for the longitudinal component of the magnetic field, $B \cos \gamma$. The evolution of magnetic flux density qualitatively follows that of $V_{integrated}$, as mentioned above.

A polarimetric analysis of the dead-calm region (see Martínez González et al. 2012b) in FoV_{QS}, used as a control box for comparison, is presented in Figure 3. This region of very quiet Sun entered the IMaX FoV after the first 200 s of the EG evolution. In Figure 3 (top panels) we present the maps of the integrated signal of $V_{measured}$, at the same representative times shown for FoV_{EG} in Figure 2 (second column). No new

magnetic structures are seen to emerge during the analyzed time series. Figure 3 (bottom panel) shows a plot of the mean polarization signal $|V_{integrated}|$ averaged over FoV_{EG} (black symbols) within the region of interest occupied by the EG inside FoV_{EG} (red symbols), and over FoV_{QS} (empty circles), along the sequence. The signal in FoV_{EG} is on average 2.7 times stronger than in FoV_{QS}. Moreover, the polarization signal in FoV_{QS} remains almost constant during the time series, while in FoV_{EG} it shows an enhancement that is even more evident in the region of interest occupied by the EG, which is correlated with the magnetic flux increase. This demonstrates that the field emergence in the EG is significant.

Figure 4 displays the evolution of two parameters that describe the EG: the magnetic flux content (top), and area (bottom). To obtain these quantities, for each frame we have defined the region of interest occupied by the EG within the IMaX FoV_{EG} by hand-drawn contours. There is, of course, a certain degree of subjectivity in defining such a region of interest, because of (i) the choice of the instant at which the preexisting structure can be definitely considered to be split into two or more descendant granules, and (ii) the possible inclusion of some adjacent pixels of the internetwork that do not belong to the structure. Nonetheless, the subjectivity in our procedure does not significantly alter the results of the present analysis, as we found when we repeated the analysis and included some additional pixels or removed some of them. Arrays containing the indices of the pixels within the hand-drawn contours have been stored to allow future replication of the analysis.

The total (unsigned) magnetic flux content of the emerging structure grows up to 4×10^{18} Mx, where Mx = 10^{-8} Wb is the CGS unit of magnetic flux, at its maximum expansion (see Figure 4, top panel). From the slope of the curve, we find a steeper increase during the first 400 s (1.5×10^{18} Mx), then a more gradual trend, and finally, a smoother increase that begins at 700 s and lasts until the end of the observations. Note that our assumption of unity filling factor has no impact on the

estimate of the magnetic flux density and on the total flux content. In Figure 4 (bottom panel) we plot the area over which magnetic flux emerges. The EG covers an area of 8–10 Mm^2, with a monotonic increase that is almost linear in time, reaching a maximum value of about 12 Mm^2. The values for the diameter of the EG (obtained under the assumption that it has an ideal circular shape) fall in the range of about 4″–5″, comparable with those reported in the literature for EGs.

3.1. Polarization Signatures

In this subsection we analyze in detail the polarization signatures present across the EG in order to characterize its magnetic configuration and to study their spatial distribution in the area of the EG.

The crosses that are plotted in Figure 2 indicate individual pixels whose Stokes profiles are shown in Figure 5. In addition, the presence of these marks allows us to perceive some slight apparent displacements of their position between the $V_{\rm integrated}$ maps and the magnetic flux density maps. This is the case, for instance, for position H. It appears just in the middle between two patches of opposite polarity in the $V_{\rm integrated}$ map, while it appears to be located just inside the positive polarity in the magnetic flux density map. Similarly, the cross relevant to position L at the center of the four descendant granules also appears at the center of the intergranular lanes with positive polarity in the map of magnetic flux density, whereas it seems to be displaced to the bottom left direction in the $V_{\rm integrated}$ map. This is due to the fact that the Stokes $V_{\rm measured}$ signal, and thus the $V_{\rm integrated}$ quantity, is altered by the small contribution brought by Stokes $U_\odot$.

In Figure 5 we plot the polarization profiles for each of the 12 positions indicated in Figure 2. In the upper panels of each set of four panels referring to a given solar location, we display the observed and fitted Stokes I and the Stokes $V_{\rm measured}$ together with the linear combination described in Equation (2), which is constructed with the superposition of the fitted Stokes Q and V parameters ($U_{\rm fitted}$ and $V_{\rm fitted}$, respectively). Furthermore, in the lower panels we separately plot the Stokes $U_{\rm fitted}$ and $V_{\rm fitted}$ profiles emerging from the SirUV inversions.

In general, that the agreement between the observed data and the fitted profiles is rather good, in particular for Stokes I profiles. Many $V_{\rm measured}$ profiles (positions A, B, F, G, and J) are fitted with a strongly dominant Stokes V component, the Stokes $U_{\rm fitted}$ signal lying entirely below three times the noise level. By contrast, some strongly asymmetric $V_{\rm measured}$ profiles are well understood in terms of superposition of Stokes $V_{\rm fitted}$ with a significant Stokes $U_{\rm fitted}$ signal. This is clearly the case of the profiles relevant to positions D and E, and to a lesser extent of those found at positions H and L. The profiles observed at positions C, I, and K represent an intermediate case because the Stokes $U_{\rm fitted}$ signal required to fit the measured data reaches just above the noise threshold.

These examples also show that, indeed, the SirUV code mainly assigns the wavelength-symmetric part of the Stokes $V_{\rm measured}$ profile to $U_{\rm fitted}$ and the antisymmetric part to $V_{\rm fitted}$. This is the case even though gradients are allowed in $v_{\rm LOS}$ and B (they have a linear dependence on τ in the inversion), so that in principle, asymmetric Stokes V profiles can be generated (e.g., Illing et al. 1975; Grossmann-Doerth et al. 1988; Solanki 1989). Nonetheless, they might be interpreted in terms of a transversal component of the field, i.e., requiring a significant Stokes $U_{\rm fitted}$ signal to fit the

Stokes $V_{\rm measured}$ profiles. This happens because the code is supplied with only two independent Stokes parameters and is therefore unable to determine the inclination and cannot distinguish between the asymmetry introduced by LOS gradients or the contribution of Stokes U signals generated by a transversal component.

As can be seen in Figure 6, the distribution of the Stokes signals across the EG clearly indicates the presence of horizontal fields in the feature. In fact, some regions with Stokes $U_{\rm fitted}$ signals above three times the noise level, shown in green, are located in bright parts of the EG. Others are found next to neutral lines, close to the edges of adjacent red and blue contours, which indicate regions with a Stokes $V_{\rm fitted}$ signal larger than three times the noise level with positive (negative) polarity. In particular, large $U_{\rm fitted}$ signals are found around the neutral line, being located at about 5″ × [4″, 6″].

3.2. Thermodynamical Parameters

The capabilities of the SirUV code, which includes full radiative transfer, allow us to study the thermodynamical parameters in the region of the solar atmosphere where flux emergence is taking place. In order to compare the thermal and pressure stratification in the EG containing the emerging flux region with those found in the undisturbed photosphere, we have studied the thermodynamical properties in FoV$_{\rm EG}$ and FoV$_{\rm QS}$ (see Figure 1).

In Figure 7 we plot the evolution of the average values of T at two optical depths ($\log \tau = 0$ and $\log \tau = -1.5$) for the entire subFoVs (left panels) and for granular (blue) and intergranular regions (red) separately (right panels). Note that before $\Delta t \approx 250$, the very quiet Sun region in FoV$_{\rm QS}$ was outside the IMaX full FoV.

The graphs indicate that the temperature at $\log \tau = 0$ is basically the same in the emerging flux region and in the very quiet Sun, except for a modestly lower value in the intergranular lanes in FoV$_{\rm QS}$. Instead, at $\log \tau = -1.5$, we find an increase of T in FoV$_{\rm EG}$ during the evolution of the emerging flux region, with a subsequent smaller decrease after $\approx$700 s. There is also a difference with respect to the very quiet region: the maximum spread is around 100 K in intergranular regions, whereas it has a lower value in granules.

In Figure 8 (left panels) we show the trend of the gas pressure averaged in FoV$_{\rm EG}$ and FoV$_{\rm QS}$ at two optical depths ($\log \tau = 0$ and $\log \tau = -1.5$). The magnetic and total (gaseous + magnetic at $\log \tau = -1.5$) pressure values in the EG region are also displayed.

The plots in Figure 8 (left panels) exhibit some fluctuations of $P_{\rm gas}$ with time. The rms variations of $P_{\rm gas}$ are about 5% for $\log \tau = 0$ and about 3% for $\log \tau = -1.5$. Furthermore, they reveal that magnetic pressure due to the emerging field increases the total pressure by about 5% at $\log \tau = -1.5$. This seems to be in agreement with the higher pressure expected in EGs for their expansion. By contrast, the pressure in the very quiet Sun region has a stationary trend.

Figure 8 (right panels) shows the same quantities for granules (blue color scheme) and intergranular lanes (red color scheme) separately. Both granular and intergranular regions are affected by the presence of the magnetic field, even if the effect on intergranules is slightly more pronounced. In these areas we also observe larger fluctuations with time. In these graphs we again find at $\log \tau = -1.5$ an increase in total pressure, which is stronger in intergranular lanes.
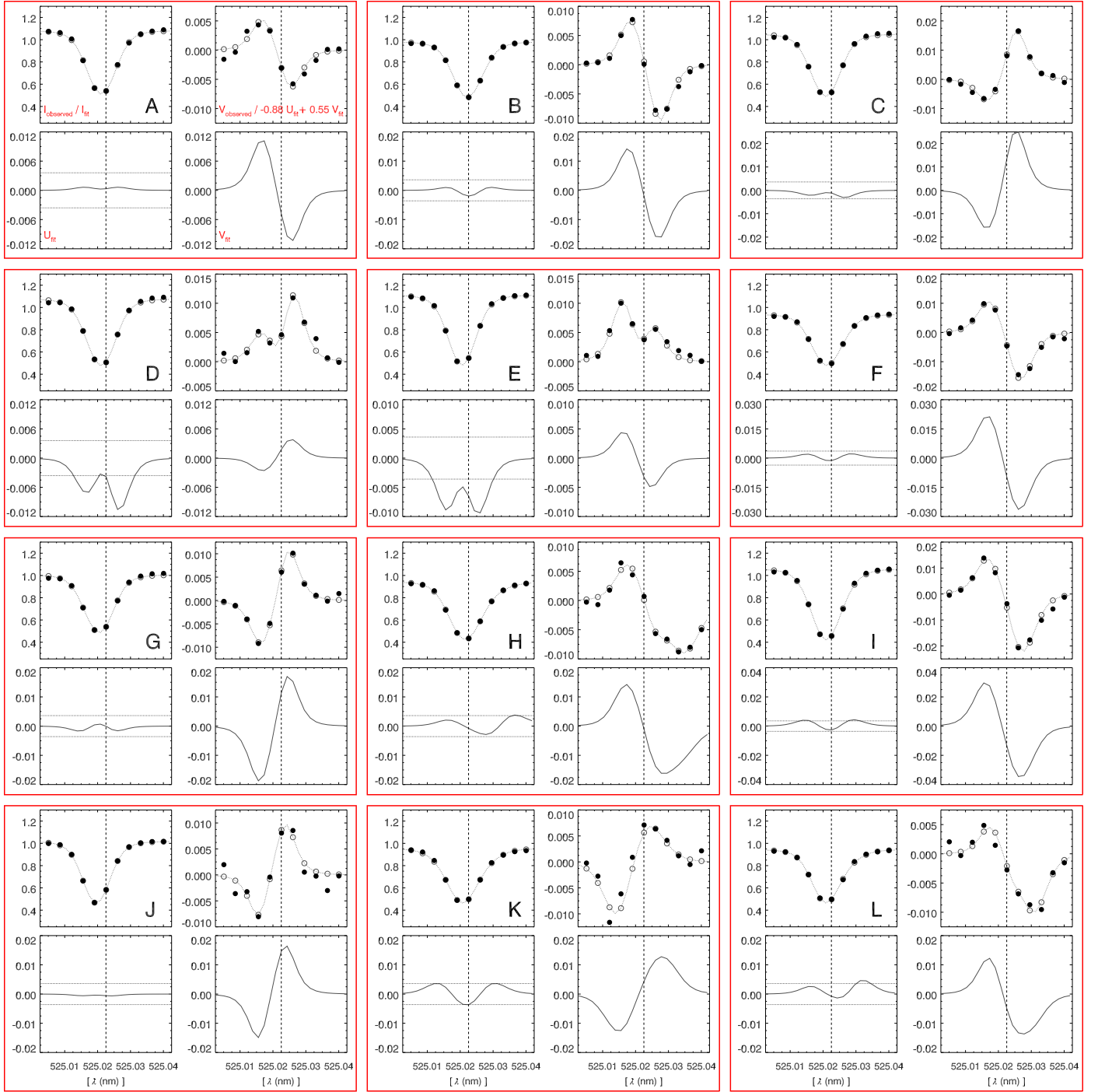
Figure 5. Stokes profiles for the positions indicated with capital letters in Figure 2. A set of four panels represents the profiles at a given position. Thus, at each spatial position, we plot Stokes *I* (upper left panel) and the linear combination represented by Equation (2) (upper right panel): filled circles represent the observed data, and empty circles represent the fitted values obtained from the SirUV inversions. The dotted line is a spline interpolation of the fitted value. Furthermore, the graph displays the fitted profiles of Stokes *U* (lower left panel) and Stokes *V* (lower right panel). The dashed lines plotted over the Stokes *U* profiles indicate three times the value of the noise.

In Figure 9 we compare the gaseous and the total pressure for the entire FoV_{EG} and for the region of interest occupied by the EG within the same subFoV, defined by the hand-drawn contours that we used before to derive the plots shown in Figure 4. The graph in Figure 9 illustrates that during the first 400 s, the total pressure is more enhanced mainly above and directly around the EG than in the neighboring granules contained in FoV_{EG}.

Note that T, P_{gas}, and P_{mag} are shown at a given optical depth τ for each pixel. However, this τ refers to very different

values of geometrical height z at different times or in different pixels that have different Wilson depressions due to the presence of the magnetic field. In particular, this occurs in areas with distinct properties such as granules and intergranular lanes.

To study these effects, we therefore compared our results with a numerical model and determined how strongly the $\log \tau = 0$ and $\log \tau = -1.5$ surfaces move up and down in such a datacube and how much the pressure varies in response

Polarization signal distribution   Δt = 504 s
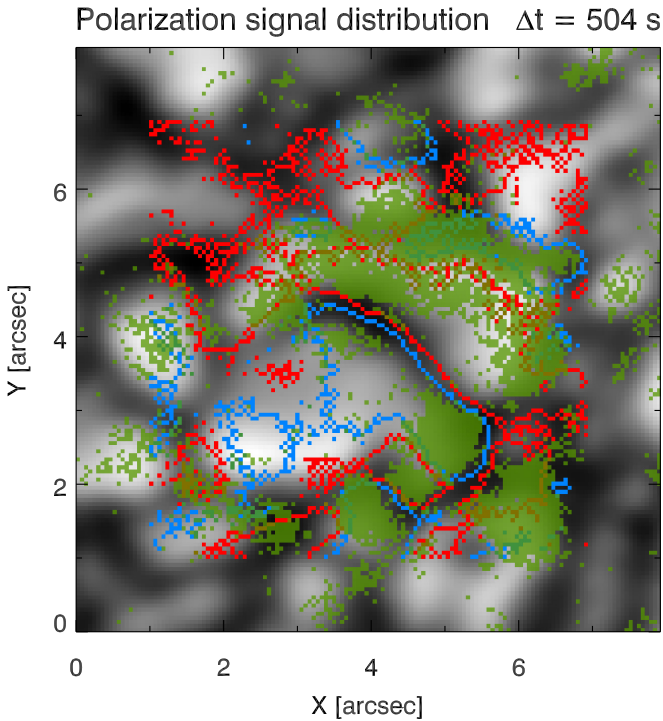
Figure 6. Distribution of the polarization signals across the EG at a given time ($\Delta t = 504$ s) during its evolution. Red (blue) contours enclose areas with V_{fitted} larger than three times the noise level, with positive (negative) polarity. Green regions indicate areas with U_{fitted} larger than three times the noise level.

to these height changes alone. We have used a snapshot from a three-dimensional nonideal compressible radiation MHD simulation calculated with the MURaM code (Vögler et al. 2005), with a unipolar seed of homogeneous vertical magnetic field of 30 G representing the quiet Sun. The data cubes cover 6 Mm in both horizontal directions, with a cell size of about 10.4 km (0″14 px^{-1}), while in the vertical direction, they extend 1.4 Mm with a 14 km cell size (for further details, see Riethmüller et al. 2014).

On average, $\log \tau = 0$ and $\log \tau = -1.5$ for the continuum at 500 nm are reached at about $z_1 = 875$ km and $z_2 = 1100$ km above the bottom boundary, respectively. The rms variations of z are $\sigma_{z_1} = 38$ km for $\log \tau = 0$ and $\sigma_{z_2} = 34$ km for $\log \tau = -1.5$.

At fixed $\log \tau$, the rms variations of P_{gas} are about 10% for $\log \tau = 0$ and about 9% for $\log \tau = -1.5$. Conversely, at geometrical heights z_1 and z_2, the rms variations of P_{gas} are about 18% and 24%, respectively. If P_{gas} is evaluated at $z_1 + \sigma_{z_1}$ and $z_1 - \sigma_{z_1}$, it changes by a slightly larger factor of 20%; similarly, P_{gas} changes by a factor of 30% when it is evaluated at $z_2 + \sigma_{z_2}$ and $z_2 - \sigma_{z_2}$. Accordingly, the fluctuations and the slight decrease in pressure with respect to the very quiet Sun that we observe during the evolution of the EG might be of stochastic origin.

Nevertheless, to further explore this issue, we have studied the horizontal components of the pressure gradient. First, we have computed these values at fixed optical depths, $\log \tau = 0$ and $\log \tau = -1.5$. Then, we have calculated the gradients at fixed geometrical heights, those corresponding to the former values of τ, i.e., 875 km and 1100 km, respectively. At $\log \tau = 0$, the change in the module of gradients between

isosurfaces of $\log \tau$ and of z_1 is relatively modest, leading to slightly smaller gradients at iso-τ. Interestingly, this implies that the pressure variation being induced by the geometrical shift of the $\log \tau = 0$ layer causes a decrease in the pressure gradient, likely due to the strong dependence of the optical depth on the gas density. This is supported by the fact that the rms of P_{gas} is smaller at iso-τ than at iso-z. At $\log \tau = -1.5$, the difference between iso-z_2 and iso-τ is larger, with significant smaller gradients at iso-τ.

We have also evaluated the angle between the horizontal gradients at iso-z and iso-τ to determine whether the signs of these gradients are preserved. In general, the majority of signs is preserved (i.e., angle $<90°$), in particular at $\log \tau = 0$. Thus, at this height, about 25% of the pixels have gradients that differ by angles between $0°$ and $15°$, while for about 72% of the pixels, the gradients at equal τ and at equal z have the same sign. At $\log \tau = -1.5$, the gradients differ by angles between $0°$ and $15°$ in about 17% of the pixels, with the gradients having the same sign in about 65% of all the pixels.

In order to compare these results with our observations, we have degraded the simulations, making a pixel four times larger to compare it to the spatial size of the pixel of the IMaX measurements. We have further convolved the pressure with a Gaussian with a full width at half-maximum (FWHM) of about 0″3, to mimic the spatial resolution of the observations, and finally, we have derived the gradients.

In general, we find smoother and smaller variations in the degraded simulations. At iso-τ, the rms variations of the degraded P_{gas} are about 6.5% for $\log \tau = 0$ and about 5% for $\log \tau = -1.5$. At iso-z_1 and iso-z_2, the rms variations of P_{gas} are about 7% and 12%, respectively. Conversely, if P_{gas} is evaluated at $z_1 \pm \sigma_{z_1}$ and $z_2 \pm \sigma_{z_2}$, it changes by 20% and 30%, similar to the original simulations.

In Figure 10 we compare the histograms of the relative frequency of the values found in the degraded simulations, at iso-τ and iso-z, and in the observations, at fixed $\log \tau$. At $\log \tau = 0$, the change between iso-z_1 and iso-τ in simulations is still modest, but slightly larger than in the case of original simulations. By contrast, there is substantial agreement between the modulus of the horizontal gradients at iso-τ in simulations and observations. Hence, when the different spatial resolution is properly taken into account, the histograms relevant to the degraded simulations look more similar to the observations. At $\log \tau = -1.5$, the difference between iso-z_2 and iso-τ in simulations is by far larger and ever smaller gradients are found in IMaX observations. This difference may have to do with problems in the simulations, although it might also be caused by the fact that SIR assumes hydrostatic equilibrium, which becomes an increasingly poorer approximation at increasing atmospheric heights.

The histogram displayed in Figure 11 illustrates that the majority of signs between the gradients calculated at iso-z and iso-τ surfaces is also preserved in the degraded simulations, in particular at $\log \tau = 0$. At this height, about 16% of the pixels have gradients that differ by angles between $0°$ and $15°$, and about 66% of the pixels have the same sign. At $\log \tau = -1.5$, about 11% of the pixels differ by angles between $0°$ and $15°$, and about 57% of the pixels have the same sign.

In conclusion, this analysis suggests that at least in part, the observed variations of P_{gas} may have a physical origin.
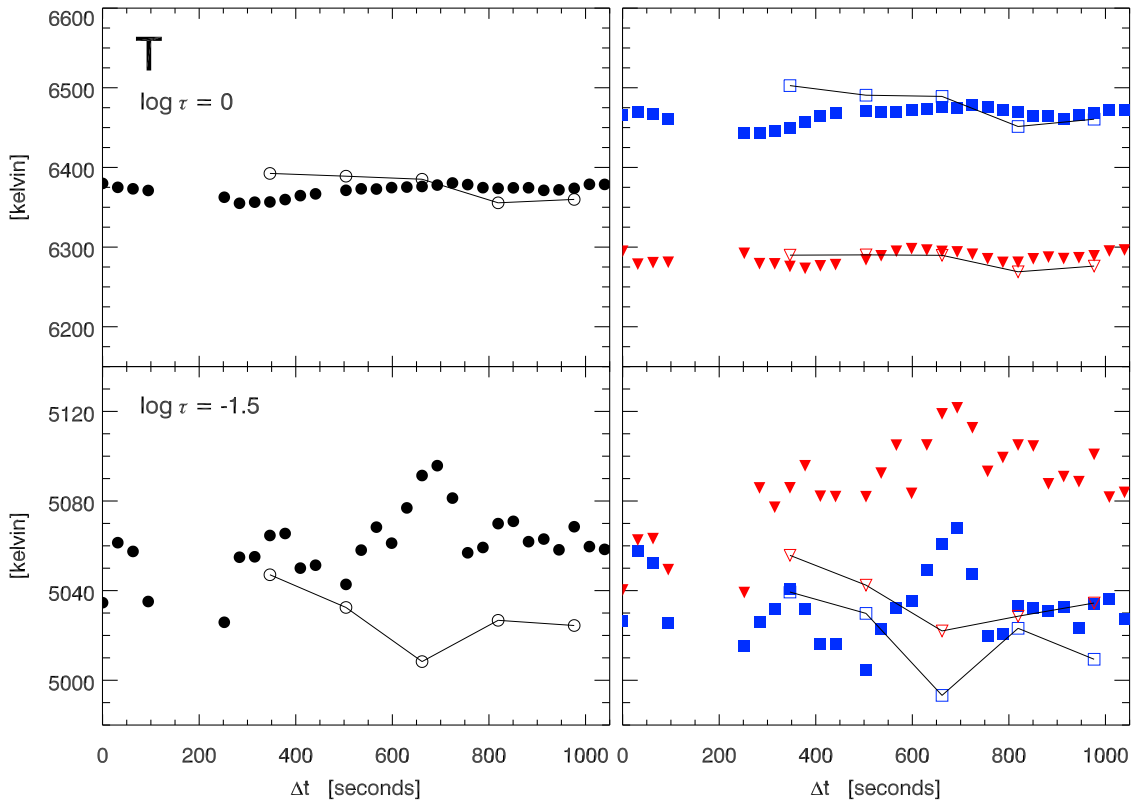
Figure 7. Left panels: evolution of the temperature (black circles) averaged within FoV$_{\mathrm{EG}}$ (solid box in Figure 1), and of T (empty circles) averaged within FoV$_{\mathrm{QS}}$ (dashed box in Figure 1) at $\log \tau = 0$ (top) and $\log \tau = -1.5$ (bottom). Right panels: same for granular (blue squares) and intergranular (red triangles) regions, respectively, present in both subFoVs.

4. Discussion

The evolution of continuum intensity maps of the EG shown in Figure 2 and in the online movie clearly indicates that we observe a so-called active granule, i.e., one that splits multiple times (see Oda 1984). The diameter reaches values of 4″–5″, in agreement with the values found in previous studies.

Across this structure, magnetic flux emergence occurs. Evidence of this is given by the appearance of adjacent mixed-polarity patches expanding along the horizontal direction. Moreover, these patches generally have upward motions. The magnetic flux brought into the photosphere is about 10^{18} Mx. The corresponding maximum value of the total unsigned flux (2×10^{18} Mx) places this solar feature at the frontier with the smallest ephemeral regions (see van Driel-Gesztelyi & Green 2015).

Remarkably, we have hints of the existence of linear polarization signals in individual locations of the feature. In fact, the plots that are displayed in Figure 4 point out that Stokes U profiles well above the noise level are required in certain pixels to fit the observed quantity V_{measured}, which is affected by cross-talk with Stokes $U_{\odot}$. In addition, the distribution of significant Stokes U_{fitted} over the EG (see Figure 6) suggests that a large part of the structure contains transverse fields. This evidence was not observed by Palacios et al. (2012), who did not take into account the cross-talk present in these IMaX L12-2 measurements. The only caveat is that some gradients of v_{LOS} and B might have been interpreted in terms of transverse fields by the SirUV code.

Concerning the thermodynamical properties of the EG, in Figures 7–9 we have presented plots of T, P_{gas}, and P_{mag} derived from the atmospheric model retrieved by the SirUV

code. They suggest that in the observed EG, the gas pressure is slightly lower than in the very quiet Sun. More importantly, they make visible that the total pressure (gaseous + magnetic) increases by at least 5% with respect to the very quiet Sun. Therefore, the magnetic field seems to provide an additional source for the horizontal expansion of the EG.

However, we cannot exclude that a fraction of the field could be in the lanes surrounding the EG, which would stop the granule from expanding. Moreover, we are able to evaluate the pressure at iso-τ, rather than at iso-z, as would be required for analyzing magnetohydrostatic equilibrium in the structure. Thus, we cannot dismiss the possibility that the higher pressure at given τ might also arise because τ moves somewhat in height when there is a magnetic field. In our description, we also neglect dynamic pressure, which may play an important role in the evolution of large granules that may not be in hydrostatic equilibrium. Indeed, the horizontal flows in granules produce a force on their surrounding gas that acts similarly to pressure from one direction, which is higher for EGs than for ordinary granules (see, e.g., Ploner et al. 1999). Last, we note that our estimate of the magnetic pressure does not take the contribution of B_{tran} fully into account, which cannot be evaluated with this IMaX measurements, although it is expected to be significant and initially larger than B_{long} in the emerging flux region.

For their part, numerical simulations predict that at the sites of flux emergence, the additional magnetic pressure is able to sustain the horizontal expansion velocity of the granules, giving rise to abnormal granulation (Cheung et al. 2007, 2008, 2010; Martínez-Sykora et al. 2008; Tortosa-Andreu & Moreno-Insertis 2009; Nóbrega-Siverio et al. 2016). Abnormal
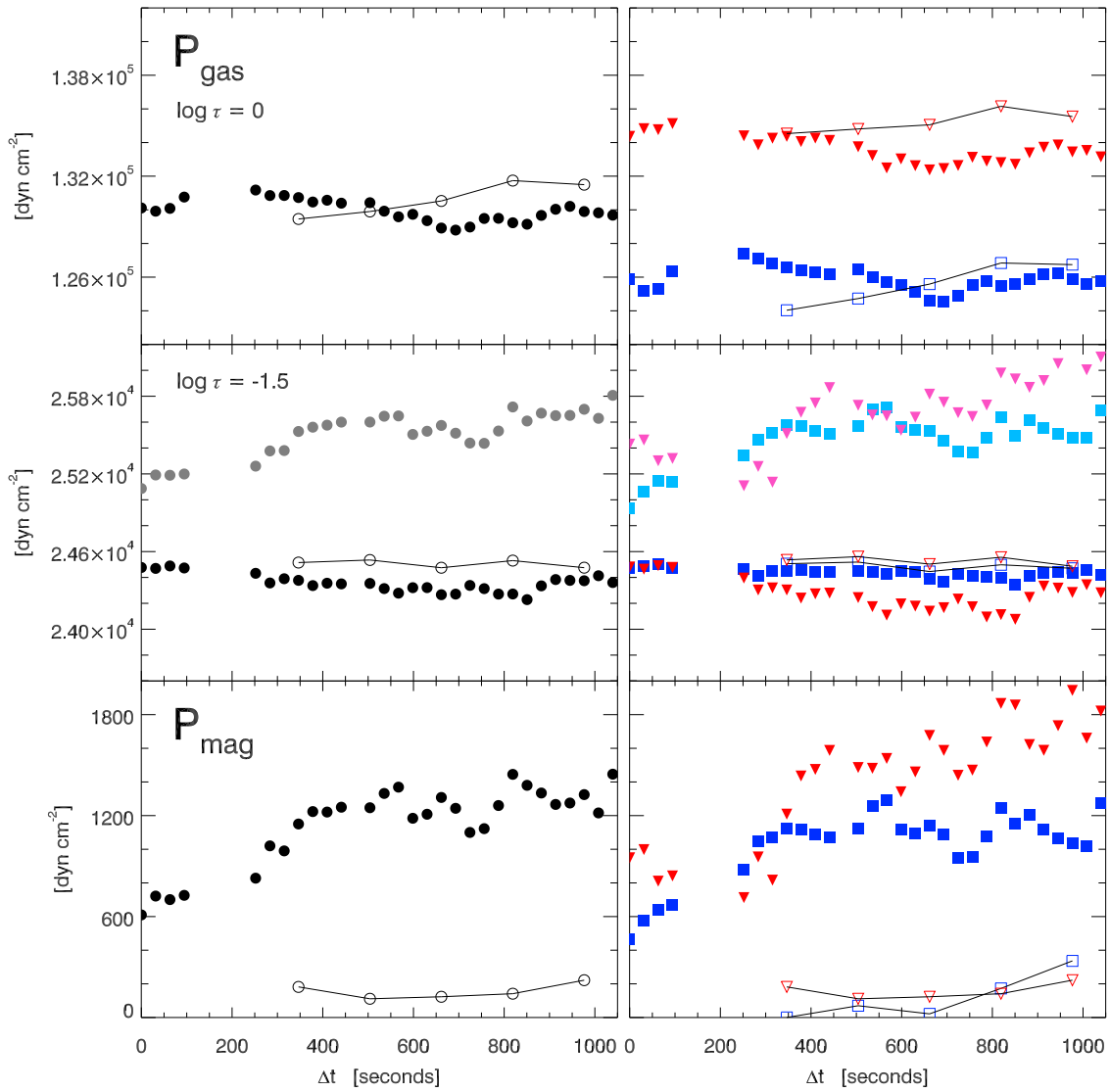
Figure 8. Left panels: evolution of the gas pressure (black circles) and of total pressure (gray circles) averaged within FoV$_{EG}$ (solid box in Figure 1), and of P_{gas} (empty circles) averaged within FoV$_{QS}$ (dashed box in Figure 1) at log $\tau = 0$ (top) and log $\tau = -1.5$ (middle). The trend of P_{mag} is also shown (bottom), for FoV$_{EG}$ (black circles) and FoV$_{QS}$ (empty circles). Right panels: same for granular (squares, blue color scheme) and intergranular (triangles, red color scheme) regions, respectively, present in both subFoVs. In the middle right panel, the light blue squares and pink triangles refer to the total pressure.
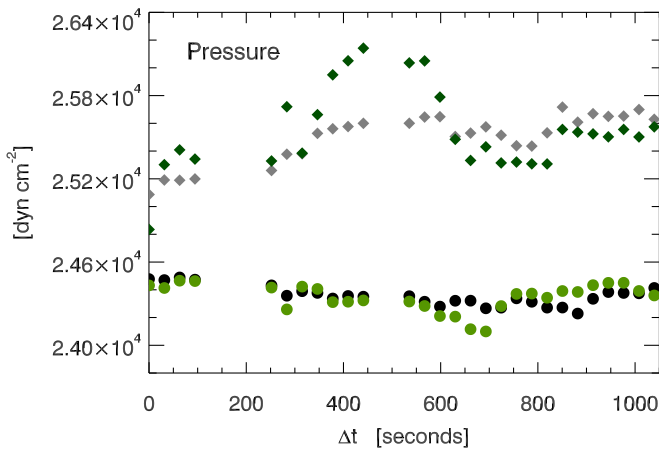
Figure 9. Evolution of the gas pressure (circles) and of total pressure (diamonds) averaged within the entire FoV$_{EG}$ (black and gray) and within the region of interest occupied by the EG inside FoV$_{EG}$ (light and dark green).

granulation was found in high-resolution observations of bipolar flux emergence (e.g., Otsuji et al. 2007; Orozco Suárez et al. 2008; Guglielmino et al. 2010; Ortiz et al. 2014; Vargas Domínguez et al. 2014; Guglielmino et al. 2018; see also the review of Cheung & Isobe 2014).

In connection with these findings, we can compare our results with those of Cheung et al. (2007) and Tortosa-Andreu & Moreno-Insertis (2009). In particular, Cheung et al. (2007) used the MURaM code to carry out radiative MHD simulations of the emergence of magnetic flux tubes, using gray radiative transfer. In their simulation of a "weak" flux tube, with initial field strength at the tube axis of 2500 G and total longitudinal flux of 3.1×10^{18} Mx, they observed that the emergence of this magnetic flux tube does not lead to a severe disturbance in the appearance of the granulation. At the site of emergence, they found the existence of predominantly horizontal fields with strengths of up to 400 G, having a rise velocity of 1–2 km s^{-1}. Moreover, the morphology of the emerged field resembles a salt-and-pepper pattern, displaying a mixture of positive and negative
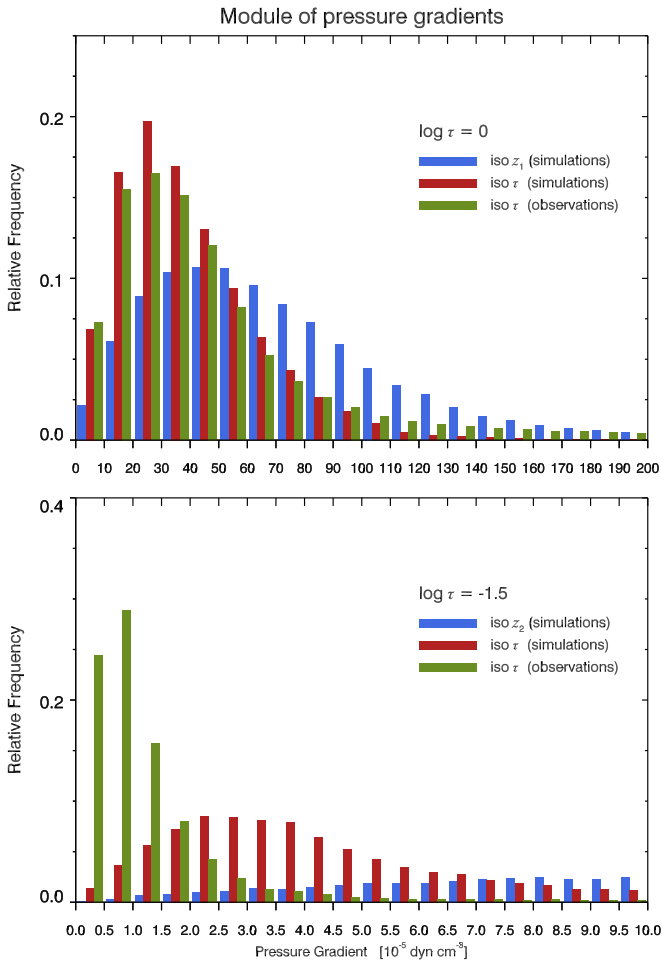
Figure 10. Top panel: histograms of the modulus of the horizontal gradients of the pressure for $\log \tau = 0$, obtained at iso-τ and iso-z in degraded simulations and at iso-τ in observations in $\mathrm{FoV_{EG}}$. Bottom panel: same for $\log \tau = -1.5$.
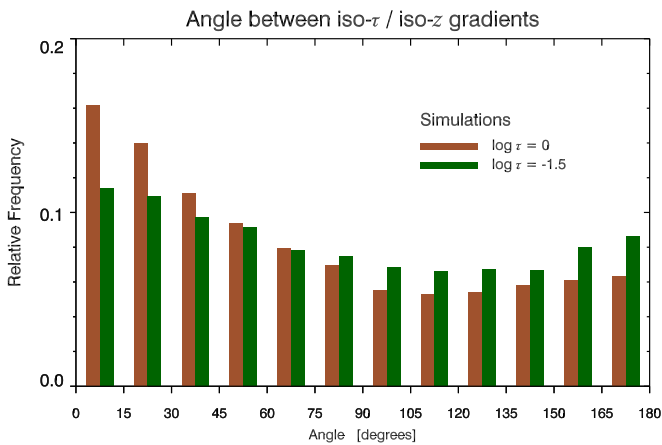
Figure 11. Angle between horizontal gradients of the pressure at fixed optical depth and at fixed geometrical height in the degraded simulations, relevant to $\log \tau = 0$ and $\log \tau = -1.5$.

small-scale flux in the intergranular network. The flux contained in each individual polarity of the emerging flux concentration is about 8×10^{17} Mx. This occurs because the flux tube is not sufficiently buoyant to rise coherently against the convective flows and fragments, leading to recirculation and overturning of material in the near-surface layers of the convection zone.

Such characteristics are qualitatively in agreement with our IMaX observations, but in these simulations, the granulation pattern seems to remain almost undisturbed.

For their part, Tortosa-Andreu & Moreno-Insertis (2009) used the MURaM code to model the emergence of magnetized plasma across granular cells in the low solar atmosphere, including radiative transfer and a detailed equation of state. In their horizontal-tube experiment, with total longitudinal flux of 3.8×10^{19} Mx, magnetized granules appear at the photosphere as isolated cells with upward velocity and grow in about 8 minutes, reaching a maximum size of $7.5\,\mathrm{Mm}^2$, which is much larger than nonmagnetic granules. Upon arrival in the photosphere, the magnetic field is predominantly horizontal, with vertical footpoints in the intergranular lanes. Then, the anomalous granules begin to fragment, and two magnetic patches with vertical field of positive and negative polarity, respectively, appear in their interior. In the meantime, intergranules become increasingly more populated with vertical-field elements. Finally, fragmentation occurs like in normal granules, with the onset of downflow and the appearance of intergranular lanes that cut across the cells. The lifetime of the anomalous granulation is about 15 minutes. Moreover, in anomalous granular cells, the total pressure reaches a peak that is 20% larger than in normal granules, which is due to the magnetic pressure that is present in the magnetized granules.

All of these values are compatible with our findings, except for the order-of-magnitude difference in magnetic flux. The value of the horizontal expansion velocity found in these MHD simulations (about 4–6 km s^{-1}) is also slightly higher than but still comparable with that obtained from our IMaX observations, about 1 km s^{-1}. This estimate was reported by Palacios et al. (2012), who calculated it for the same emergence event from geometrical considerations and from flow maps of various quantities using a local correlation-tracking method.

Recently, using high-resolution MHD simulations of a photospheric small-scale dynamo performed with the MURaM code, Rempel (2018) analyzed the amplification of magnetic field in EGs. This study focused on the time evolution of newly formed downflow lanes in the centers of EGs, finding that horizontal flows converging toward the lanes can amplify an initially weak vertical field of about a few 10 G up to 800 G within a few minutes. This field is organized in extended narrow magnetic sheets whose length is comparable to the granular scale. This process appears to be due to the contributions of both shallow and deep recirculation. In particular, the deep recirculation seems to be linked to strong sheet-like structures, coupling the magnetic field that reaches the photosphere in the centers of EGs to the deeper convection zone, while the shallow recirculation provides the primary source for the subsequent appearance of small-scale turbulent fields in the downflow lanes.

In the numerical simulations of Rempel (2018), upflow regions are dominated by a horizontal field. When deep recirculation is allowed, the average values for $|B_z|$ and $|B_h|$ at $\log \tau = 0$ in these upflow regions are 50 G and 100 G, respectively. Field amplification in the downflow lanes leads to average values of 130 G and 160 G for $|B_z|$ and $|B_h|$, respectively. In an attempt to compare our observational results with these numerical findings, we have calculated the average value of $|B_z| \equiv |B_{\mathrm{long}}|$ at $\log \tau = 0$ within the EG. Figure 12 shows the trend of $\langle |B_z| \rangle$ for the entire area of the EG (black
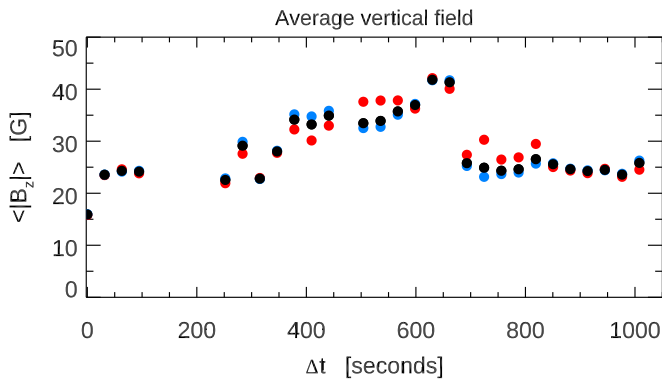
Figure 12. Evolution of the average absolute value of the longitudinal component of the magnetic field in the emerging structure cospatial to the EG (black symbols). Blue and red symbols refer to the average values in regions with upflows or downflows, respectively.

symbols) and for the upflow and downflow regions (blue and red symbols). We find that $\langle |B_z| \rangle$ is stronger in the upflow regions during the first phases of the analyzed EG, whereas at later times, $\langle |B_z| \rangle$ becomes stronger in the downflow regions. We also note a resemblance of the numerical results to our observations in the shape of the magnetic sheet cospatial to the central downflow lanes observed at $\Delta t = 504$ s in Figure 2. Nonetheless, one has to be cautious when comparing the numerical values from the study of Rempel (2018) with the observed values, which appear to fall short of the former. Indeed, it would be necessary to degrade the results of simulations to mimic the spatial resolution of the IMaX observations. Moreover, due to the lack of full spectro-polarimetric measurements, we are not able to estimate the value of the horizontal field $|B_h|$, which is expected to be dominant in the EG.

In this context, it is important to mention that recently, Moreno-Insertis et al. (2018) identified the formation of organized horizontal magnetic sheets covering whole granules in realistic three-dimensional magnetoconvection models of small-scale flux emergence. In this regard, Fischer et al. (2019) reported on the first clear observational evidence of a magnetic sheet emergence, characterizing its development. Moreno-Insertis et al. (2018) also provided a rough estimate for the occurrence of sheet-like events of between 0.3 and 1 day^{-1} Mm^{-2}. Given the IMaX FoV (about $46'' \times 46''$) and the duration of the time series ($\approx$20 minutes of stable pointing), with an intermediate frequency value of 0.5 day^{-1} Mm^{-2}, we would expect to observe about eight events. However, we only found this single event in the IMaX L12-2 time series.

Emergence events with horizontal, i.e., very inclined magnetic fields, such as the one we investigated here, might in some way be related with HIFs, as already suggested by De Pontieu (2002). Indeed, Lites et al. (2008) reported on HIFs organized on a mesogranular scale. The presence of such a cellular pattern on a scale of $5''$–$10''$ was confirmed by Ishikawa & Tsuneta (2010), who further linked the transient horizontal fields to the emergence of granular-scale horizontal fields, advected by mesogranular flows (see also Ishikawa & Tsuneta 2011). Mesogranular boundaries were found to be the preferential location of magnetic elements (Yelles Chaouche et al. 2011), in particular at the site of convectively driven sinks (Requerey et al. 2017), as also reported in simulations of small-scale dynamo action in the quiet Sun (e.g., Bushby & Favier 2014). In addition, cluster emergence of

mixed polarities in the internetwork, carrying a flux amount of about 10^{18} Mx, was observed by Wang et al. (2012).

The origin of these magnetic structures may reside in weakly twisted magnetic fields, which do not survive into the photosphere as coherent flux bundles. This is shown in numerical models of flux tubes rising from the bottom of the convection zone (Moreno-Insertis et al. 1995; Magara 2001; Toriumi & Yokoyama 2010; Martínez-Sykora et al. 2015). The remnant fields can be recycled by magnetoconvection to form internetwork fields. Alternatively, the remnants of decaying active regions can be also recycled, as suggested by Ploner et al. (2001). Nonetheless, this is surely not the case in these IMaX observations, which were taken during the long solar minimum in 2008–2010. As a third option, the generation of such emergence events with horizontal fields in the quiet Sun may be ascribed to a turbulent local dynamo process occurring in the near-surface layers (see, e.g., Vögler & Schüssler 2007; Rempel 2014; Borrero et al. 2017, and references therein). In this case, these small-scale magnetic fields might not have a relationship with the global dynamo, even though recent dynamo simulations indicate that the small-scale dynamo mechanism and the large-scale field are tangled (Karak & Brandenburg 2016).

5. Conclusions

IMaX/Sunrise observations of the solar photosphere taken at disk center have revealed a number of small-scale episodes of magnetic flux emergence (see, e.g., Danilovic et al. 2010; Solanki et al. 2010, 2017; Guglielmino et al. 2012, and references therein).

Here, we have studied the emergence phase of a magnetic structure, extending over the mesogranular scale, that was cospatial with an EG. We have analyzed the polarization maps and then inverted the Stokes profiles with the SIR code to obtain information on the physical parameters of the magnetic structure. Our study reveals that this feature hosts linear polarization patches and brings an excess of total pressure (gaseous + magnetic) into the photosphere.

The overall characteristics suggest that we observe an emerging multipolar magnetic flux-sheet structure that seems to be able to disturb the granulation pattern. The detection of this feature is made possible by the high polarimetric sensitivity of IMaX.

Our findings are in agreement with numerical simulations of flux emergence at small scales, some of which indicate the presence of anomalous granular cells in these sites. This could also be the case for some EGs, such as the EG we analyzed here: when the incipient granule carries a magnetic field of sufficient intensity, the additional push of the magnetic pressure might lead to the formation of cells that are larger than usual. A magnetic field strength of about the equipartion value with the kinetic energy of photospheric plasma flows, $\approx$400 G (see, e.g., Solanki et al. 1996; Ishikawa et al. 2008), seems to be necessary to see these disturbances in the granulation (Cheung et al. 2007).

Indeed, state-of-the-art simulations do not clearly show if the amount of flux carried by the structure that we observe is enough to modify the granulation pattern. The emergence event studied with our IMaX observations appears to have characteristics intermediate between those found in the MHD numerical experiments of Cheung et al. (2007) and those of Tortosa-Andreu & Moreno-Insertis (2009). This points out that simulations of

emergence of such amounts of flux are needed to properly interpret solar features such as the feature presented here. In addition, we note that recent numerical models of flux emergence including magnetoconvection have shown the existence of small-scale magnetic sheets that at maximum development cover granular surfaces (Moreno-Insertis et al. 2018).

However, we cannot rule out the possibility that we also partly see weak fields that were present earlier (Lamb et al. 2008, 2010), as discussed in Gošić et al. (2016). These might become concentrated by the shuffling motions due to the EG and in this way become visible. For instance, this seems to occur in the EG studied by Fischer et al. (2017). Moreover, we should also consider the possibility that the presence of the EG, which may have a large upflow under it, helps the magnetic flux to emerge at its location, rather than the emerging field driving the evolution of the EG.

In order to verify whether EGs have a magnetic nature, it would be worthwhile to study the frequency of flux emergence events that are cospatial with EGs, to determine how often they occur. Such an endeavour could start by determining whether other EGs present in IMaX observations, taken during both the first and the second SUNRISE flights, are associated with emerging flux. More in general, full spectropolarimetric measurements with high spectral resolution would be a more straightforward approach for identifying the presence of horizontal fields associated with EGs. The high spatial resolution, high polarimetric sensitivity, and long temporal coverage provided by the PHI instrument (Solanki et al. 2015, 2020) on board the Solar Orbiter space mission (Müller et al. 2013) will surely enhance our capability of finding these events and will increase the statistics for such a study. To this purpose, it will be mandatory to use an effective segmentation algorithm for pattern recognition to identify EGs in solar granulation and compare their location with horizontal flux emergence events. In this context, a method used to detect families of splitting granules such as the method developed by Roudier et al. (2003, 2016) to study families of fragmenting granules appears to be more promising than classical approaches based on edge or intensity levels, such those described, e.g., by Berrilli et al. (2005) and Falco et al. (2017). Finally, multiline measurements would also allow analyzing the thermodynamical properties in more detail at different atmospheric heights.

New investigations on the properties of these structures are required to answer the question about their origin and to reach a unified understanding of their dynamics. In particular, the analysis of the frequency of these emergence events in correlation with the solar cycle will provide a clearer picture of their sources. This will be achieved by using data from the PHI instrument as well as from the large-aperture ground-based telescopes Daniel K. Inouye Solar Telescope, DKIST (Keil et al. 2010), and the European Solar Telescope, EST (Collados et al. 2010).

Appendix

We have carried out a series of preliminary runs to test the reliability of the SirUV inversions. We have taken 2000 atmosphere models, randomly chosen from those obtained from the inversions of an IMaX V5-6 data set (see Guglielmino et al. 2012). To avoid the tendency of the inversions that retrieve horizontal fields for pixels at noise level (see, e.g., Asensio Ramos 2009; Stenflo 2010; del Toro Iniesta & Ruiz Cobo 2016), we have imposed the condition that the original inclination had to be $\gamma < 80°$ or $\gamma > 100°$ in order for the model to be included in the set. These models have been used as input for the synthesis of 2000 profiles of Stokes I, U, and V. The range used for the stratification is $-4.0 < \log \tau < 1.4$, where τ is the optical depth at 500 nm. The computed synthetic profiles have been convolved with the spectral point-spread function at the focal plane of IMaX. Moreover, we have added random noise to these synthetic profiles, which corresponds to the signal-to-noise ratio for these IMaX V5-6 measurements, about 1×10^{-3} in units of I_c per wavelength point in each Stokes parameter.

As the next step, we have generated the linear combination represented by Equation (2) using the synthetic Stokes U and V parameters. This computed profile and the Stokes I profile have been sampled at the same wavelength positions used in the
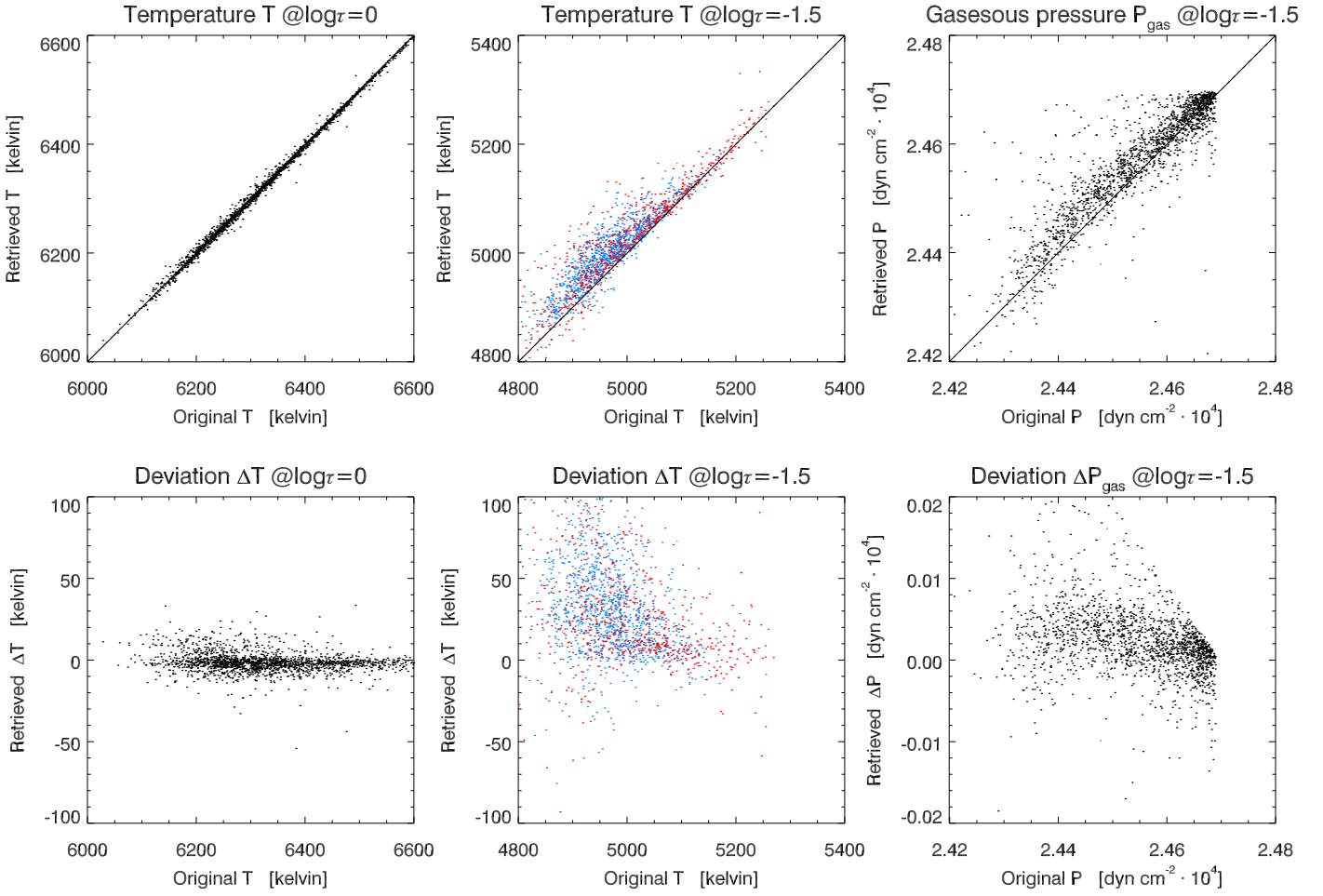
Figure A1. Top: scatter plots of the temperature retrieved by the SirUV code vs. the original atmospheric value (see main text for more details) at $\log \tau = 0$ (left) and $\log \tau = -1.5$ (middle) and the same for the gas pressure at $\log \tau = -1.5$ (right). Bottom: the deviations between the original atmospheric value and the values retrieved by the inversions for the same quantities as above. Blue (red) points refer to original atmospheric models with $B < 100$ G ($B > 100$ G).

L12-2 observing mode. Then, we have provided the SirUV code with these simulated data, inverting the Stokes I profile and the linear combination in Equation (2). The Harvard Smithsonian Reference Atmosphere (HSRA; Gingerich et al. 1971) has been used as initial guess for the temperature stratification. For the inversion, we have used three iteration cycles, with up to four nodes for the temperature T, two nodes for the LOS velocity v_{LOS} and B, and one node for the other parameters. No filling factor is taken into account in the inversion. The total number of free parameters is nine for the SirUV inversions, with a total number of 24 data points to be considered.

Finally, for each simulated and inverted profile, we have compared the original atmospheric values and those retrieved by the SirUV inversion. We have also computed the deviation Δ between these values for several atmospheric parameters: T, electronic pressure, gas pressure P_{gas}, microturbulent velocity, v_{LOS}, B, γ, and azimuth angle ϕ. The values of v_{LOS} and B have been averaged between $\log \tau = -1$ and $\log \tau = -2$, where the response functions are more sensitive. We have further examined the longitudinal and transverse components of the magnetic field, $B \cos \gamma$ ($=B_{long}$) and $B \sin \gamma$ ($=B_{tran}$), respectively.

Figure A1 (top panels) displays the scatter plots of the temperature versus the original value at two different values of

$\log \tau$, namely $\log \tau = 0$ (left) and $\log \tau = -1.5$ (middle). We find a very good agreement between the temperature derived by the SirUV code and the original temperature at $\log \tau = 0$. At this height, their deviation ΔT is about a few tens of kelvin (see Figure A1, bottom left panel). The agreement is also satisfactory at $\log \tau = -1.5$. In this case, we note a modest difference between the two populations: profiles emerging from atmospheric models with originally $B < 100$ G (blue points) present a slightly larger positive deviation than profiles with originally $B > 100$ G (red points). However, ΔT is not higher than 100 K and can be neglected (Figure A1, bottom central panel). The scatter plot of P_{gas} at $\log \tau = -1.5$ is also shown (Figure A1, top right panel). The original and inverted values of P_{gas} also agree fairly well. For this parameter, the deviations are about 0.5% (Figure A1, bottom right panel). Similar results are obtained for the electronic pressure and the microturbulent velocity.

In Figures A2 and A3 we show the scatter plots for other physical quantities, their deviations, and the frequency histograms of the deviations.

Figure A2 presents the graphs for the total magnetic field strength B (first column) and for the components $B \cos \gamma$ (second column) and $B \sin \gamma$ (third column). The magnetic field strength plots indicate considerable scatter and a tendency of the SirUV inversions to overestimate the value
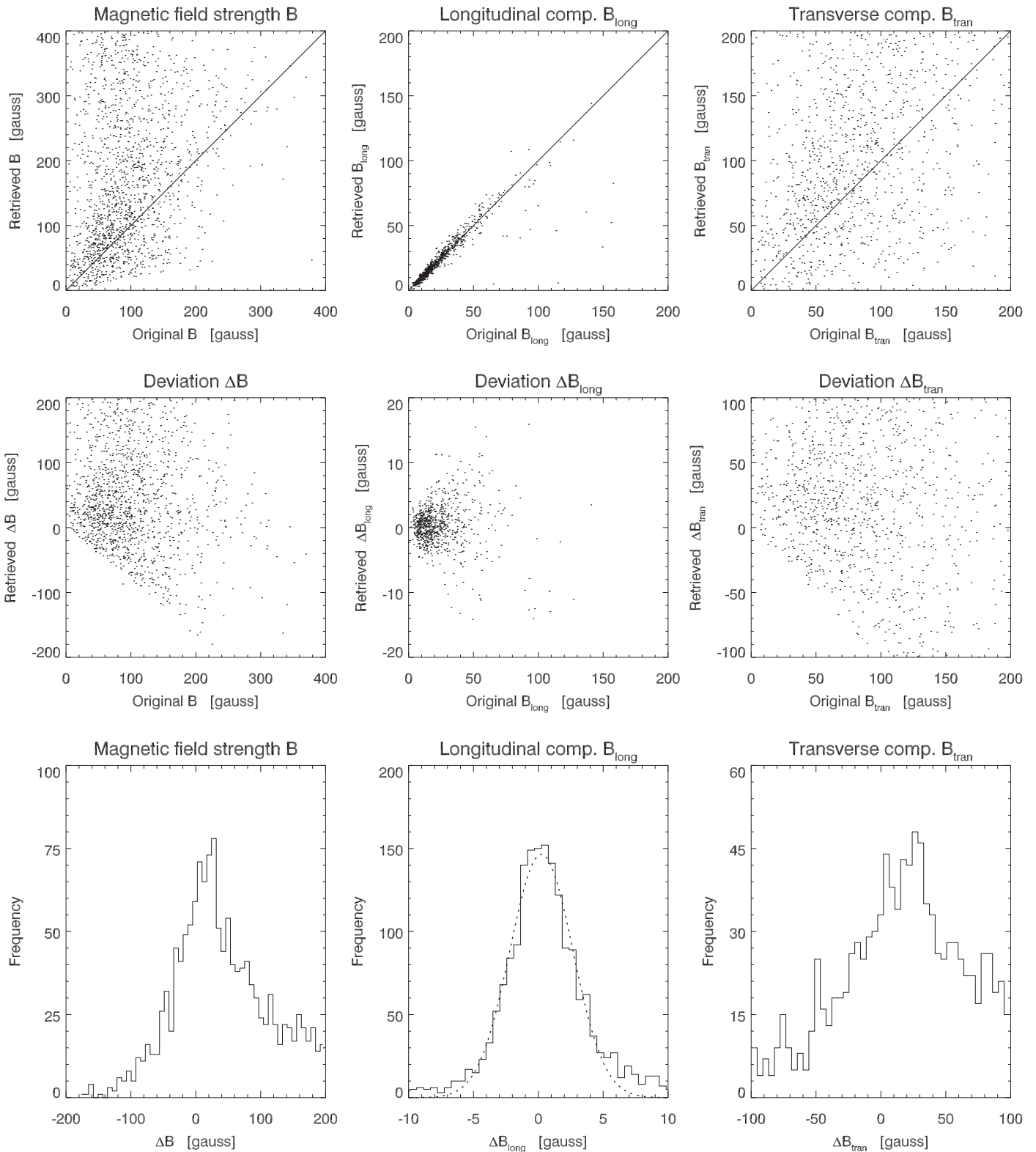
Figure A2. Top: scatter plots of B (left), B_{long} (middle), and B_{tran} (right) retrieved by the SirUV code vs. the original atmospheric values (see main text for more details). Middle: the deviations between the original atmospheric value and the values retrieved by the inversions for these quantities. Bottom: the corresponding frequency histograms for the differences plotted in the middle row. The dashed line overplotted on the histogram of B_{long} represents a Gaussian fit to the data.

of B. This may depend on the noise in the data (Borrero & Kobel 2011, 2012). The longitudinal component B_{long} exhibits an excellent agreement between the original and inverted values. The deviation has a symmetric, very narrow Gaussian profile, as can be seen from Figure A2

(bottom middle panel). The FWHM is about 5.7 G. In contrast, the transverse component shows a very wide scatter. This leaves B_{tran} totally undetermined. We note that for the magnetic field and its components, there is no dependence on the values of the original values of B. The
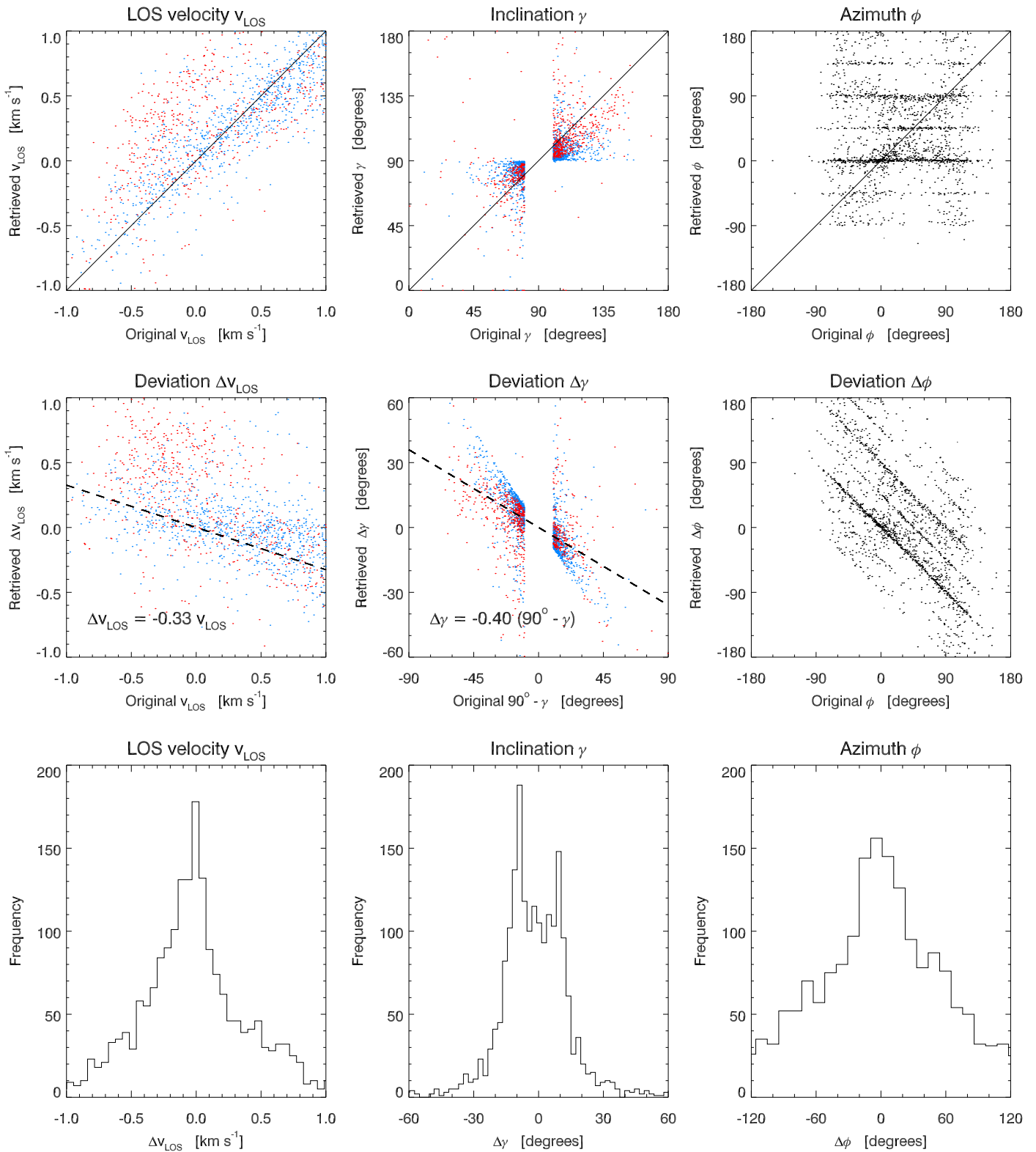
Figure A3. Same as in Figure A2, but for v_{LOS}, γ, and ϕ. Blue (red) points refer to original atmospheric models with $B < 100$ G ($B > 100$ G). The dashed lines overplotted on the deviation of v_{LOS} and γ represent a linear fit to the data.

large uncertainty in B_{tran} is not surprising because the full Stokes vector is not measured, which is further compounded by the relatively small number of sampled wavelength points. This is also the main reason for the large uncertainty in determining B.

Figure A3 displays the plots for v_{LOS} (first column), γ (second column), and ϕ (third column). For v_{LOS} and γ, we again find the difference in the scatter plots between the inversions of profiles with original $B < 100$ G (blue points) and those with $B > 100$ G (red points). The LOS velocity is

slightly better retrieved for profiles with weaker original field strength. For profiles with $B < 100\,\mathrm{G}$, we find a linear relation between v_{LOS} and Δv_{LOS}

$$\Delta v_{\mathrm{LOS}} = -0.33\,v_{\mathrm{LOS}},$$

with an estimated error on the coefficient of ± 0.01. The histogram of the cumulative deviations for v_{LOS} has a roughly symmetric profile (Figure A3, bottom left panel). The best-fitting Gaussian distribution has a FWHM of about $0.74\,\mathrm{km\,s^{-1}}$. As far as the inclination is concerned, we note a general tendency of the inversions to retrieve a value of γ that is more horizontal than the original value. This behavior is reflected in the double-peaked histogram (Figure A3, bottom middle panel), which is likely an artifact produced by imposing the condition on the original inclination to be $\gamma < 80°$ or $\gamma > 100°$, and in the scatter plot of the deviation with respect to the original value of the quantity $(90° - \gamma)$ (Figure A3, central middle panel). The tendency is stronger for weaker field profiles, as is commonly found in inversions of noisy polarization signals (Borrero & Kobel 2011, 2012). For profiles with $B > 100\,\mathrm{G}$, we are able to infer a linear relation between γ and $\Delta\gamma$, which is given by

$$\Delta\gamma = -0.40\,(90° - \gamma),$$

with an estimated error on the coefficient of ± 0.03. For the sake of precision, it has to be pointed out that this formula might be affected by the restriction to original inclination $\gamma < 80°$ or $\gamma > 100°$. Last, we note that the azimuth angle also remains completely indeterminate.

This preliminary test allows us to argue that the SirUV code is able to give reliable values only for certain atmospheric parameters from the inversion of Stokes I and of the linear combination of Stokes U and V described in Equation (2). First, the code infers the correct values of the thermodynamic parameters. Indeed, this behavior of the code is expected because these physical quantities leave their mark on the Stokes I profile at least as strongly as on the other Stokes parameters. Furthermore, the SirUV code provides an excellent estimate of the longitudinal component of the magnetic field, $B\cos\gamma$.

Somewhat surprisingly, we obtain a poor estimate for v_{LOS}, which is better recovered for profiles with weaker original field strength. This fact reflects that in these profiles, the LOS velocity is mainly inferred from the Stokes I parameter, with limited disturbance due to the signal of Stokes $U_\odot$. This alters the Stokes V signal. The code also gives inadequate information on the values of B and γ. The former is often overestimated in comparison to the original value, the latter is more horizontal in most cases, in particular in the profiles with weaker original field that are closer to the noise level and have weaker Stokes V signals. Finally, the transverse component of the magnetic field and ϕ remains completely undetermined.

The inability of the SirUV inversions to recover the correct values for these quantities can be easily understood. γ is fundamentally given by the ratio between the linear polarization $(\sqrt{Q^2 + U^2})$ and the circular polarization (V). Furthermore, ϕ depends on the ratio between Q and U. Provided that the code is not supplied with independent information on the linear and circular polarization, in particular, it totally lacks knowledge of Stokes Q, it cannot estimate these physical parameters in a reliable manner. Conversely, the longitudinal component of the magnetic field is basically dependent on V,

which is entirely supplied to the code via the linear combination described in Equation (2).

In conclusion, the SirUV code eliminates the effect of the residual polarization cross-talk in V_{measured} as far as the measurements of the longitudinal flux are concerned. Thus, the magnetic flux density can be correctly evaluated. We note that we have carried out these tests by choosing only atmospheric models with an original weak field strength, $B < 500\,\mathrm{G}$ because we intended to use the SirUV code in analogous conditions over quiet-Sun internetwork regions that are observed by IMaX in our data set.

ORCID iDs

Salvo L. Guglielmino ● https://orcid.org/0000-0002-1837-2262
Basilio Ruiz Cobo ● https://orcid.org/0000-0001-9550-6749
Luis R. Bellot Rubio ● https://orcid.org/0000-0001-8669-8857
José Carlos del Toro Iniesta ● https://orcid.org/0000-0002-3387-026X
Tino L. Riethmüller ● https://orcid.org/0000-0001-6317-4380
Francesca Zuccarello ● https://orcid.org/0000-0003-1853-2550

References

Allen, M. S., & Musman, S. 1973, SoPh, 32, 311
Anusha, L. S., Solanki, S. K., Hirzberger, J., & Feller, A. 2017, A&A, 598, A47
Asensio Ramos, A. 2009, ApJ, 701, 1032
Barthol, P., Gandorfer, A., Solanki, S. K., et al. 2011, SoPh, 268, 1
Berkefeld, T., Schmidt, W., Soltau, D., et al. 2011, SoPh, 268, 103
Berrilli, F., Consolini, G., Pietropaolo, E., et al. 2002, A&A, 381, 253
Berrilli, F., del Moro, D., Russo, S., et al. 2005, ApJ, 632, 677
Borrero, J. M., Jafarzadeh, S., Schüssler, M., & Solanki, S. K. 2017, SSRv, 210, 275
Borrero, J. M., & Kobel, P. 2011, A&A, 527, A29
Borrero, J. M., & Kobel, P. 2012, A&A, 547, A89
Bushby, P. J., & Favier, B. 2014, A&A, 562, A72
Carlier, A., Chauveau, F., Hugon, M., & Rösch, J. 1968, CRASB, 266, 199
Cheung, M. C. M., & Isobe, H. 2014, LRSP, 11, 3
Cheung, M. C. M., Rempel, M., Title, A. M., & Schüssler, M. 2010, ApJ, 720, 233
Cheung, M. C. M., Schüssler, M., & Moreno-Insertis, F. 2007, A&A, 467, 703
Cheung, M. C. M., Schüssler, M., Tarbell, T. D., & Title, A. M. 2008, ApJ, 687, 1373
Collados, M., Bettonvil, F., Cavaller, L., & Team, E. S. T. 2010, AN, 331, 615
Danilovic, S., Beeck, B., Pietarila, A., et al. 2010, ApJL, 723, L149
De Pontieu, B. 2002, ApJ, 569, 474
del Toro Iniesta, J. C., & Ruiz Cobo, B. 2016, LRSP, 13, 4
Domínguez Cerdeña, I. 2003, A&A, 412, L65
Dravins, D., Lindegren, L., & Nordlund, A. 1981, A&A, 96, 345
Falco, M., Puglisi, G., Guglielmino, S. L., et al. 2017, A&A, 605, A87
Fischer, C. E., Bello González, N., & Rezaei, R. 2017, A&A, 602, L12
Fischer, C. E., Borrero, J. M., Bello González, N., et al. 2019, A&A, 622, L12
Gadun, A. S., Hanslmeier, A., Pikalov, K. N., et al. 2000, A&AS, 146, 267
Gandorfer, A., Grauf, B., Barthol, P., et al. 2011, SoPh, 268, 35
Gingerich, O., Noyes, R. W., Kalkofen, W., & Cuny, Y. 1971, SoPh, 18, 347
Gošić, M., Bellot Rubio, L. R., del Toro Iniesta, J. C., Orozco Suárez, D., & Katsukawa, Y. 2016, ApJ, 820, 35
Grossmann-Doerth, U., Schüssler, M., & Solanki, S. K. 1988, A&A, 206, L37
Guglielmino, S. L., Bellot Rubio, L. R., Zuccarello, F., et al. 2010, ApJ, 724, 1083
Guglielmino, S. L., Martínez Pillet, V., Bonet, J. A., et al. 2012, ApJ, 745, 160
Guglielmino, S. L., Zuccarello, F., Young, P. R., Murabito, M., & Romano, P. 2018, ApJ, 856, 127
Hirzberger, J. 2002, A&A, 392, 1105
Hirzberger, J., Bonet, J. A., Vázquez, M., & Hanslmeier, A. 1999a, ApJ, 515, 441

Hirzberger, J., Bonet, J. A., Vázquez, M., & Hanslmeier, A. 1999b, ApJ, 527, 405

Hirzberger, J., Koschinsky, M., Kneer, F., & Ritter, C. 2001, A&A, 367, 1011

Hirzberger, J., Vázquez, M., Bonet, J. A., Hanslmeier, A., & Sobotka, M. 1997, ApJ, 480, 406

Illing, R. M. E., Landman, D. A., & Mickey, D. L. 1975, A&A, 41, 183

Ishikawa, R., & Tsuneta, S. 2010, ApJL, 718, L171

Ishikawa, R., & Tsuneta, S. 2011, ApJ, 735, 74

Ishikawa, R., Tsuneta, S., Ichimoto, K., et al. 2008, A&A, 481, L25

Jafarzadeh, S., Cameron, R. H., Solanki, S. K., et al. 2014, A&A, 563, A101

Jafarzadeh, S., Solanki, S. K., Feller, A., et al. 2013, A&A, 549, A116

Karak, B. B., & Brandenburg, A. 2016, ApJ, 816, 28

Kawaguchi, I. 1980, SoPh, 65, 207

Keil, S. L., Rimmele, T. R., Wagner, J. & ATST Team 2010, AN, 331, 609

Kitai, R., & Kawaguchi, I. 1979, SoPh, 64, 3

Lagg, A., Solanki, S. K., Riethmüller, T. L., et al. 2010, ApJL, 723, L164

Lamb, D. A., DeForest, C. E., Hagenaar, H. J., Parnell, C. E., & Welsch, B. T. 2008, ApJ, 674, 520

Lamb, D. A., DeForest, C. E., Hagenaar, H. J., Parnell, C. E., & Welsch, B. T. 2010, ApJ, 720, 1405

Landi Degl'Innocenti, E. 1992, in Solar Observations: Techniques and Interpretation, ed. F. Sanchez, M. Collados, & M. Vazquez (Cambridge: Cambridge Univ. Press), 71

Lites, B. W., Kubo, M., Socas-Navarro, H., et al. 2008, ApJ, 672, 1237

Lites, B. W., Leka, K. D., Skumanich, A., Martínez Pillet, V., & Shimizu, T. 1996, ApJ, 460, 1019

Magara, T. 2001, ApJ, 549, 608

Martínez González, M. J., Bellot Rubio, L. R., Solanki, S. K., et al. 2012a, ApJL, 758, L40

Martínez González, M. J., Manso Sainz, R., Asensio Ramos, A., & Hijano, E. 2012b, ApJ, 755, 175

Martínez Pillet, V., del Toro Iniesta, J. C., Álvarez-Herrero, A., et al. 2011, SoPh, 268, 57

Martínez-Sykora, J., Hansteen, V., & Carlsson, M. 2008, ApJ, 679, 871

Martínez-Sykora, J., Moreno-Insertis, F., & Cheung, M. C. M. 2015, ApJ, 814, 2

Massaguer, J. M., & Zahn, J.-P. 1980, A&A, 87, 315

Matloch, L., Cameron, R., Schmitt, D., & Schüssler, M. 2009, A&A, 504, 1041

Matloch, L., Cameron, R., Shelyag, S., Schmitt, D., & Schüssler, M. 2010, A&A, 519, A52

McClure, R. L., Rast, M. P., & Martínez Pillet, V. 2019, SoPh, 294, 18

Mehltretter, J. P. 1978, A&A, 62, 311

Moreno-Insertis, F., Caligari, P., & Schüssler, M. 1995, ApJ, 452, 894

Moreno-Insertis, F., Martinez-Sykora, J., Hansteen, V. H., & Muñoz, D. 2018, ApJL, 859, L26

Müller, D., Marsden, R. G., St., Cyr, O. C., & Gilbert, H. R. 2013, SoPh, 285, 25

Musman, S. 1972, SoPh, 26, 290

Namba, O. 1986, A&A, 161, 31

Namba, O., & Diemel, W. E. 1969, SoPh, 7, 167

Namba, O., & van Rijsbergen, R. 1977, Problems of Stellar Convection, Lecture Notes in Physics, Vol. 71 (Berlin: Springer), 119

Nelson, G. D., & Musman, S. 1978, ApJL, 222, L69

Nóbrega-Siverio, D., Moreno-Insertis, F., & Martínez-Sykora, J. 2016, ApJ, 822, 18

Nordlund, Å. 1985, SoPh, 100, 209

Nordlund, Å., Stein, R. F., & Asplund, M. 2009, LRSP, 6, 2

November, L. J., Toomre, J., Gebbie, K. B., & Simon, G. W. 1981, ApJL, 245, L123

Oda, N. 1984, SoPh, 93, 243

Orozco Suárez, D., Bellot Rubio, L. R., del Toro Iniesta, J. C., & Tsuneta, S. 2008, A&A, 481, L33

Ortiz, A., Bellot Rubio, L. R., Hansteen, V. H., de la Cruz Rodríguez, J., & Rouppe van der Voort, L. 2014, ApJ, 781, 126

Otsuji, K., Shibata, K., Kitai, R., et al. 2007, PASJ, 59, S649

Palacios, J., Blanco Rodríguez, J., Vargas Domínguez, S., et al. 2012, A&A, 537, A21

Ploner, S. R. O., Schüssler, M., Solanki, S. K., & Gadun, A. S. 2001, in ASP Conf. Ser. 236, Advanced Solar Polarimetry—Theory, Observation, and Instrumentation, ed. M. Sigwarth (San Francisco, CA: ASP), 363

Ploner, S. R. O., Solanki, S. K., & Gadun, A. S. 1999, A&A, 352, 679

Ploner, S. R. O., Solanki, S. K., & Gadun, A. S. 2000, A&A, 356, 1050

Rast, M. P. 1995, ApJ, 443, 863

Rast, M. P. 2003, ApJ, 597, 1200

Rempel, M. 2014, ApJ, 789, 132

Rempel, M. 2018, ApJ, 859, 161

Requerey, I. S., del Toro Iniesta, J. C., Bellot Rubio, L. R., et al. 2014, ApJ, 789, 6

Requerey, I. S., del Toro Iniesta, J. C., Bellot Rubio, L. R., et al. 2015, ApJ, 810, 79

Requerey, I. S., del Toro Iniesta, J. C., Bellot Rubio, L. R., et al. 2017, ApJS, 229, 14

Riethmüller, T. L., & Solanki, S. K. 2017, A&A, 598, A123

Riethmüller, T. L., Solanki, S. K., Berdyugina, S. V., et al. 2014, A&A, 568, A13

Rieutord, M., Roudier, T., Malherbe, J. M., et al. 2000, A&A, 357, 1063

Rösch, J. 1960, in IAU Symp. 12, Aerodynamic Phenomena in Stellar Atmospheres, ed. R. N. Thomas (Cambridge: Cambridge Univ. Press), 313

Roth, M., Franz, M., Bello González, N., et al. 2010, ApJL, 723, L175

Roudier, T., Eibe, M. T., Malherbe, J. M., et al. 2001, A&A, 368, 652

Roudier, T., Lignières, F., Rieutord, M., Brandt, P. N., & Malherbe, J. M. 2003, A&A, 409, 299

Roudier, T., Malherbe, J. M., Rieutord, M., & Frank, Z. 2016, A&A, 590, A121

Roudier, T., & Muller, R. 2004, A&A, 419, 757

Ruiz Cobo, B., & del Toro Iniesta, J. C. 1992, ApJ, 398, 375

Simon, G. W., Title, A. M., & Weiss, N. O. 1991, ApJ, 375, 775

Simon, G. W., & Weiss, N. O. 1991, MNRAS, 252, 1P

Sobotka, M., del Moro, D., Jurčák, J., et al. 2012, A&A, 537, A85

Socas-Navarro, H., Martínez Pillet, V., & Lites, B. W. 2004, ApJ, 611, 1139

Solanki, S. K. 1989, A&A, 224, 225

Solanki, S. K., Barthol, P., Danilovic, S., et al. 2010, ApJL, 723, L127

Solanki, S. K., del Toro Iniesta, J. C., Woch, J., et al. 2015, Polarimetry, 305, 108

Solanki, S. K., del Toro Iniesta, J. C., Woch, J., et al. 2020, A&A, in press

Solanki, S. K., Riethmüller, T. L., Barthol, P., et al. 2017, ApJS, 229, 2

Solanki, S. K., Zufferey, D., Lin, H., Rueedi, I., & Kuhn, J. R. 1996, A&A, 310, L33

Stein, R. F., & Nordlund, Å. 1998, ApJ, 499, 914

Stenflo, J. O. 2010, A&A, 517, A37

Title, A. M., Tarbell, T. D., Topka, K. P., et al. 1989, ApJ, 336, 475

Toriumi, S., & Yokoyama, T. 2010, ApJ, 714, 505

Tortosa-Andreu, A., & Moreno-Insertis, F. 2009, A&A, 507, 949

Utz, D., del Toro Iniesta, J. C., Bellot Rubio, L. R., et al. 2014, ApJ, 796, 79

van Driel-Gesztelyi, L., & Green, L. M. 2015, LRSP, 12, 1

Vargas Domínguez, S., de Vicente, A., Bonet, J. A., et al. 2010, A&A, 516, A91

Vargas Domínguez, S., Kosovichev, A., & Yurchyshyn, V. 2014, ApJ, 794, 140

Vögler, A., & Schüssler, M. 2007, A&A, 465, L43

Vögler, A., Shelyag, S., Schüssler, M., et al. 2005, A&A, 429, 335

Wang, J., Zhou, G., Jin, C., & Li, H. 2012, SoPh, 278, 299

Yelles Chaouche, L., Moreno-Insertis, F., Martínez Pillet, V., et al. 2011, ApJL, 727, L30

Yu, D., Xie, Z., Hu, Q., et al. 2011, ApJ, 743, 58

Zhang, J., Yang, S.-H., & Jin, C.-L. 2009, RAA, 9, 921